Defects in exosome biogenesis are associated with sensorimotor defects in zebrafish *vps4a* mutants

Running title: Sensorimotor defects in zebrafish *vps4a* mutants

Anna Shipman[1], Yan Gao[1], Desheng Liu[2], Shan Sun[2], Jingjing Zang[3], Peng Sun[1], Zoha Syed[1], Amol Bhagavathi[1], Eliot Smith[1,4], Timothy Erickson[5], Matthew Hill[1,6], Stephan Neuhauss[3], Sen-Fang Sui[2], Teresa Nicolson[1]

[1]Department of Otolaryngology, Stanford University, Stanford, CA, United States
[2]State Key Laboratory of Membrane Biology, Beijing Frontier Research Center for Biological Structure, Beijing Advanced Innovation Center for Structural Biology, School of Life Sciences, Tsinghua University, Beijing, China
[3]Department of Molecular Life Sciences, University of Zurich, Zurich, Switzerland
[4]Present address: Biotechne Corporation, Newark, CA United States 94304
[5]Department of Biology, University of New Brunswick, Fredericton, Canada
[6]Present address: Department of Otolaryngology, University of Colorado, Aurora, CO, United States

Corresponding author: Teresa Nicolson
Email: tnicolso@stanford.edu

Number of pages: 52
Number of figures: 7
Number of words abstract: 248
Number of words introduction: 607
Number of words discussion: 1479

Conflict of Interest Statement: The authors declare no competing financial interests.

Acknowledgements: The authors would like to thank the past members of the Genetics Department of the Max Planck Institute in Tuebingen, Germany, particularly Tatjana Piotrowski and Stefan Schulte-Merker for their assistance in a small-scale allele screen. We would also like to thank Matthew Esqueda and Sivan Brodo-Abo for their help with animal care. This work was supported in part by a National Institute on Deafness and Other Communication Disorders award (DC0170046) and SICHL funding from the OHNS department of Stanford University to T.N.; a grant from the National Natural Science Foundation of China to S.S. (92254306); Swiss National Science Foundation (310030_204648) to S.N.

Abstract

Mutations in human *VPS4A* are associated with neurodevelopmental defects, including motor delays and defective muscle tone. *VPS4A* encodes a AAA-ATPase required for membrane scission, but how mutations in *VPS4A* lead to impaired control of motor function is not known. Here we identified a mutation in zebrafish *vps4a*, T248I, that affects sensorimotor transformation. In biochemical experiments we show the T248I mutation reduces the ATPase activity of Vps4a and disassembly of its substrate, ESCRT filaments, which mediate membrane scission. Consistent with the established role for Vps4a in the endocytic pathway and exosome biogenesis, *vps4a*^{T248I} mutants have enlarged endosomal compartments in the CNS and decreased numbers of circulating exosomes. Resembling the central form of hypotonia in human *VPS4A* patients, motor neurons and muscle cells are unaffected in mutant zebrafish as touch sensitivity is intact. Unlike somatosensory function, optomotor responses, vestibulospinal (VS), and acoustic startle reflexes are severely impaired in *vps4a*^{T248I} mutants, indicating a greater sensitivity of these circuits to the T248I mutation. ERG recordings indicate that visual ability is largely reduced in the mutants, however, *in vivo* imaging of tone-evoked responses in the inner ear and ascending auditory pathway show comparable activity. Further investigation of central pathways in *vps4a*^{T248I} mutants revealed that sensory cues failed to fully activate neurons in the VS and medial longitudinal fasciculus (MLF) nuclei that directly innervate motor neurons. Our results suggest that a defect in sensorimotor transformation underlies the profound yet selective effects on motor reflexes resulting from the loss of membrane scission mediated by Vps4a.

Significance Statement

Here we present a T248I mutation in *vps4a*, which causes sensorimotor defects in zebrafish larvae. Spanning biochemical to systems level analyses, our study indicates that a reduction in Vps4a enzymatic activity leads to endosomal defects and reduced exosome biogenesis,

resulting in pronounced deficits in vision and sensorimotor transformation of auditory and vestibular cues. We suggest that the mechanisms underlying this type of dysfunction in zebrafish may also contribute to the condition seen in human patients with *de novo* mutations in the human *VPS4A* orthologue.

Introduction

Neurodevelopmental disorders are a collection of conditions that affect central nervous system growth and development and can have a wide variety of associated clinical signs, such as impaired cognition, difficulties in communication, and motor defects. Many neurodevelopmental disorders are the result of genetic mutations and often target molecular pathways that impact protein synthesis, transcriptional or epigenetic regulation or synaptic signaling (Lewis and Kroll, 2018; Cardoso et al., 2019; Parenti et al., 2020). An early feature that is common to several neurodevelopmental defects is central hypotonia (low muscle tone), however, it remains unclear how the underlying biochemical and sensorimotor mechanisms can result in this feature (Dan, 2022).

De novo heterozygous missense mutations in human Vacuolar protein sorting-associated protein 4A (*VPS4A*) have been associated with neurodevelopmental disorders characterized by pronounced delays in development, motor skills and speech, and severe intellectual disabilities and visual dysfunction (Rodger et al., 2020). Symptoms arising from problems with muscle tone such as hypotonia and dystonia are also thought to be central in nature (Ganguly et al., 2021). In addition, mutations in *VPS4A* are associated with Congenital Dyserythropoietic Anemia (Seu et al., 2020; Lunati et al., 2021). *VPS4A* encodes a type I AAA-ATPase that was originally identified in yeast. In multicellular organisms, a paralogue, *VPS4B*, is also expressed and both genes are highly conserved from plants to humans (Babst et al., 1997; Scheuring et al., 2001; Strausberg et al., 2002; Beyer et al., 2003). VPS4A binds to the

98 endosomal sorting complexes required for transport (ESCRT) fission machinery to promote
99 dissociation of the subunits via ATP hydrolysis after membrane scission occurs. Membrane
100 scission is a key step in several cellular processes including cytokinesis, neurite severing,
101 plasma membrane repair and multivesicular body formation (Babst et al., 2002; Monroe et al.,
102 2014; Alonso Y Adell et al., 2016; Ott et al., 2018). Multivesicular bodies form within the
103 endocytic pathway when late endosomes bud inward and membrane scission occurs,
104 generating small intraluminal vesicles (Piper and Katzmann, 2007; Alonso Y Adell et al., 2016;
105 Bebelman et al., 2020; Kalluri and LeBleu, 2020). During further processing, multivesicular
106 bodies can subsequently either fuse to the plasma membrane to release the intraluminal
107 vesicles as exosomes into the extracellular matrix, or fuse with lysosomes to promote
108 degradation of its contents (Dobrowolski and De Robertis, 2012; Meldolesi, 2018). Both fates of
109 intraluminal vesicles are key for maintaining cell homeostasis and signal transduction (Cocucci
110 et al., 2009; Palmulli and van Niel, 2018). In animal studies, it has been previously shown that
111 RNAi knockdown of *vps4* in fruit fly larvae results in defective pruning of neurites and knock out
112 of *Vps4a* in mice results in lethality at preweaning stages (Loncle et al., 2015; Cacheiro et al.,
113 2020). In line with the known function of VPS4A, fibroblasts from *VPS4A* human patients
114 display defects in endosomal morphology and cell division (Rodger et al., 2020). How these
115 defects lead to motor system impairment in probands is not fully understood.
116 Here, we identified a missense mutation in zebrafish *vps4a*, T248I, which was
117 generated in a small scale ENU mutagenesis screen for mutants that display auditory/vestibular
118 defects (Haffter et al., 1996). We show that the zebrafish *vps4a* mutants display endosomal
119 abnormalities and reduced numbers of exosomes in the CNS. Both defects are consistent with
120 the induction of stress response genes in mid- and hindbrain regions of *vps4a*^{T248I} mutants.
121 Using *in vivo* calcium imaging, we detected strongly reduced activity in the motor circuits
122 associated with movements evoked by sensory inputs. These findings support a model where
123 the reduced enzymatic activity of Vps4a results in a disruption in late endosome function and

124 exosome release, consequently reducing cellular homeostasis within neural circuits mediating
125 sensorimotor transformation.
126
127
128 **Materials and Methods**
129 **Zebrafish care and use**
130 We maintained zebrafish lines for the *vps4a*^{T248I} allele in the Top Long Fin (TLF) wild-type (WT)
131 or *mitfa*^{b692} *nacre* backgrounds. The *vps4a*^{T248I} Tg(α-tubulin-gal4;MP-gal4;cmlc2-GFP;UAS-
132 GCaMP7a) line was generated by crossing into a *mitfa*^{b692} Tg(α-tubulin-gal4;MP-gal4;cmlc2-
133 GFP;UAS-GCaMP7a) fish line (a gift from Philippe Mourrain). The MP-gal4 transgene was
134 present in most fish, marking the muscle cells as well. Breeding stocks were housed at 28.5°C
135 and animal husbandry followed standard zebrafish methods for laboratory utilization
136 (Westerfield, 2000), as approved and overseen by the Institutional Animal Care and Use
137 Committees at both Oregon Health and Sciences University and Stanford University. The
138 experiments used zebrafish larvae 3-7 days post fertilization (dpf) before gender differentiation
139 occurs. Embryos and larvae were raised in E3 medium (0.33 mM CaCl2, 0.17 mM KCl, 0.33
140 mM MgSO4, and 5 mM NaCl) incubated at 28.5°C. When appropriate, larvae were anesthetized
141 in E3 with 0.03% 3-amino benzoic acid ethylester (MESAB, Western Chemical) to minimize pain
142 and distress.
143
144 **Genotyping Methods**
145 For the *vps4a*^{T248I} allele, we genotyped fish and larvae using kompetitive allele-specific PCR
146 (KASP) genotyping (LGC Biosearch Technologies) per the manufacturer's instructions.
147
148 **Identification of raumschiff mutant allele**

149 Positional cloning was performed using simple sequence length polymorphism (SSLP) markers
150 mapped to the zebrafish genome (Knapik et al., 1998). 5 dpf zebrafish larvae were sorted by
151 phenotype.
152 For Whole Genome Sequencing, 5 dpf zebrafish larvae were sorted into separate pools
153 of 20 homozygous mutants and 20 heterozygous and homozygous wild-type siblings. Genomic
154 DNA was collected using a DNeasy Blood & Tissue Kit (Qiagen) and samples were processed
155 by Azenta Life Sciences (formerly GENEWIZ) for library preparation and Illumina HiSeq
156 sequencing. The resulting .gz files were uploaded to SNPTrack
157 (http://genetics.bwh.harvard.edu/snptrack/) to identify the mutation.
158
159 **CRISPR injections**
160 Single guide RNAs against *vps4a* and *vps4b* were designed using the CHOPCHOP website
161 (https://chopchop.cbu.uib.no/)(Labun et al., 2019) and synthesized (Alt-R CRISPR-Cas9
162 System, IDT). Three guides were chosen based on if they targeted the ATPase domain or
163 additional exons common to all isoforms, low number of off target sites and efficiency. Multi-
164 guide CRISPR injections were performed as described previously (Kroll et al., 2021). Briefly,
165 crRNA and tracrRNA guides were combined in equal molar amounts in Duplex Buffer (IDT), and
166 this RNA Duplex mix was combined with 1 µg/µL Cas9-NLS protein (PNA Bio). 1 nL of RNA
167 guide-CAS9 mixture was injected into single cell stage TLF wildtype embryos. Embryos were
168 checked daily for viability and auditory/vestibular phenotypes scored on 5 dpf.
169
170 **Protein expression and purification**
171 *Saccharomyces cerevisiae* Vps4 (wild-type), and mutant Vps4(T254I) were cloned into the
172 pET28a vector with an N-terminal His6 tag. The two proteins were expressed in Escherichia coli
173 BL21 (DE3) strains and induced with 1 mM IPTG at 20°C overnight. Sonication was used to lyse
174 cells and centrifuged the lysates. The supernatant was loaded into Ni–NTA beads (GE

175 Healthcare) and the eluates were incubated with 5 U mL−1 apyrase (Sigma-Aldrich) at 4°C
176 overnight. All proteins were further purified by SEC using a Superdex 200 10/300 GL column
177 (GE Healthcare) with 20 mM Tis-HCl at pH 8.0, 150 mM NaCl buffer. The purity and quality of all
178 the proteins were tested by SDS–PAGE and Nano-drop (Implen).
179 *Saccharomyces cerevisiae* Snf7 mutant (R52E) and Vps24 were cloned into the pET28a
180 vector with an N-terminal His6 tag. The two proteins were expressed in Escherichia coli BL21
181 (DE3) strains and induced with 1 mM IPTG at 20°C overnight. Sonication was used to lyse cells
182 and centrifuged the lysates. The supernatant was loaded to a Ni–NTA beads (GE Healthcare)
183 and the elute was further purified by SEC using a Superdex 200 10/300 GL column (GE
184 Healthcare) with 20 mM Tis-HCl at pH 8.0, 150 mM NaCl buffer. The purity and quality of all the
185 proteins were tested by SDS–PAGE and Nano-drop (Implen).
186 *Saccharomyces cerevisiae* Vps2 were cloned into the pET28a vector with an N-terminal
187 MBP-His6 -TEV-tag. We expressed the resulting Vps2 construct in E.coli BL21 (DE3) at 20°C
188 for 16 hours with 1 mM IPTG. We purified the protein using Ni–NTA resin (GE Healthcare). We
189 mixed the eluted fractions from the His column with TEV (tobacco etch virus) protease for 3
190 hours at 4°C. We then loaded the cleaved samples onto a 5 mL HiTrap Q-sepharose FF column
191 (GE Healthcare) and eluted the material with a gradient of 0%-100% buffer (20 mM Tris-HCl, pH
192 8.0, 500 mM NaCl) in 50 column volumes.
193
194 **Sedimentation Analysis of Filament Disassembly**
195 Yeast ESCRT III filaments were assembled by mixing Snd7(R52E), Vps24 and Vps2 in a molar
196 ratio of 2:1:1 at room temperature for 1 hour. Then, the formed filaments were centrifuged at
197 50,000 r.p.m. for 30 minutes in a TLA-100 ultracentrifuge rotor (Beckman Coulter). The pellet
198 was resuspended in the buffer containing 20 mM Tris-HCl at pH 8.0, 150 mM NaCl. The pellet
199 (P) and supernatant (S) were analyzed by SDS–PAGE.

200 For sedimentation analysis of ESCRT III filament disassembly, filaments were mixed
201 with 5 μM Vps4 or Vps4(T254I) in 20 mM Tris-HCl at pH 8.0, 150 mM NaCl, 2 mM MgCl2 buffer,
202 separately. Reactions were started by adding ATP to a final concentration of 5 mM. After
203 incubation at room temperature for 10 minutes, reactions were stopped by adding EDTA to a
204 final concentration of 50 mM. Samples were then subjected to ultracentrifugation and analyzed
205 via SDS-PAGE and negative staining.
206
207 **ATPase activity assay**
208 ATPase activities were determined for wild-type and mutant Vps4 proteins using the
209 Quantichrome ATPase/GTPase Assay Kit (BioAssay Systems) at room temperature. Briefly,
210 5 μM Vps4 or mutant Vps4(T254I) protein was added to ATPase assay buffer and 4 mM ATP for
211 30 minutes, and then stopped using reagent from the kit. The solution was incubated at room
212 temperature for 30 minutes, and immediately the absorbance at 620 nm was detected using a
213 plate reader (Enspire, Perkin Elmer). The released phosphate was calculated based on the
214 absorbance standard curve established using KH_2PO_4 standards.
215
216 **Auditory-evoked behavioral response (AEBR)**
217 AEBR was tested as described previously (Erickson et al., 2017; Smith et al., 2020) using the
218 Zebrabox system (ViewPoint Life Sciences). 5 dpf wild-type siblings or *vps4a*^{T248I} mutant larvae
219 were confined to wells of a 96-well plate in 200 μL E3 per well, in the dark. Larvae were
220 subjected to 100 millisecond, 1kHz pure tones at 157 decibel sound pressure (dB SPL, relative
221 to 1mPA) every 2 seconds for 1 minute. An infrared camera recorded larval movements and
222 ZebraLab tracking software documented pixel changes, which represent movement over time
223 for each larva. To distinguish between evoked responses and spontaneous background
224 movement, movements within 1 second before a stimulus were excluded from a given trial. For

225 each larva, the positive responses were calculated as a percentage out of total possible
226 response within a minute, and the best of three trials was used for analysis.
227
228 **Vestibulospinal Reflex (VSR)**
229 The device and method used to test the VSR was done as previously described (Sun et al.,
230 2018; Gao and Nicolson, 2021). Briefly, 5 dpf larvae were embedded dorsal-up in 2%
231 prewarmed low melt agarose in E3 media without anesthetic on a mounting chamber. The
232 agarose around the trunk and pectoral fins was carefully removed and replaced with 20 μL E3
233 media, and the mounting chamber was placed in the device. A motor rocks the platform from
234 −75° to + 75° at 0.53 Hz, and an infrared camera recorded video of the reflex at 30 fps (1280
235 frames).
236 Modified ZebraZoom software (Mirat et al., 2013) tracks the movements of the trunk at
237 regular intervals and calculates the real tail angle over time between the X axis and the axis
238 formed by the tip of the tail and the center of the swimming bladder.
239
240 **Vestibular-induced eye movement (VIEM)**
241 The VIEM experiment was done similarly as described previously using a modified device (Mo
242 et al., 2010; Sun et al., 2018). 5 dpf larvae were embedded on a small cover slip in prewarmed
243 2% low melt agarose in E3 buffer, without anesthetic. Agarose surrounding the eyes was gently
244 removed and replaced with approximately 10 μL of E3 media to permit free eye moment. The
245 mounted larvae were positioned vertically, head down, between an infrared camera and an
246 infrared LED array on a programmable rocking platform. Larvae kept in darkness during the
247 experiment. The platform rocked (-45° to 45°) at 0.25 Hz frequency for 60 seconds while larval
248 eye movements were video recorded in infrared.

249 Software-based video analyses quantified the amplitudes of angular eye movements as
250 a function of their frequency of repetition. Larvae with normal VIEM show peak movement
251 amplitude at 0.25 Hz, in synchrony with platform rotation. Baseline spontaneous eye movement,
252 taken as the average amplitude across all quantified frequencies, was subtracted to determine
253 the VIEM amplitude at 0.25 Hz. We calculated the normalized amplitude of the eye ratio for
254 each larva and used the two-tailed unpaired t test with Welch's correction to compare mutants
255 to their corresponding siblings.
256
257 **Touch Startle Reflex**
258 Touch Startle was performed by mounting 7 dpf zebrafish larvae similarly to the VSR mounting
259 method. A micromanipulator holding a borosilicate glass capillary tube (Sutter, #BF150-86-10)
260 pulled into a needle was used to touch the head of the larvae. Startle movements were
261 recorded by a Hamamatsu C11440 ORCA-Flash 2.8 camera at 100 fps. Quantification of C-
262 bends was performed as described in (Budick and O'Malley, 2000).
263
264 **Optomotor Reflex (OMR)**
265 To test for the optomotor reflex, we adapted the assay from Neuhauss et al., 1999. A set of 4
266 tracks (each lane measuring at 12 cm x 0.6 cm) and comb that fit between the lanes, was
267 constructed using 3D printing. The lanes were placed in a 15 cm petri dish (VWR) and filled
268 partially with E3 buffer. The comb was inserted to block the starting end of the lanes, and 5-6
269 dpf larvae were placed in the starting area of the lanes. The petri dish was placed over a
270 screen that plays a video of 0.5 cm stripes. To record the movement of the larva along the
271 lanes, a camera was mounted above the petri dish. To perform the experiment, the video of
272 stripes was played, and the comb was removed, allowing larva to swim against the movement
273 of stripes to the end of the lane. To quantify this reflex, screenshots of the video were taken of
274 the larva in the starting region of the lane prior to comb removal and then 30 seconds after the

275 comb was removed. The distance between the location of each larva prior to comb removal
276 and 30 seconds after was measured in ImageJ in millimeters.
277
278 **Electroretinogram (ERG)**
279 ERG recordings were performed on 5 - 6 dpf mutant and wild-type sibling larvae, as described
280 in (Makhankov et al., 2004; Niklaus et al., 2017). b-wave amplitudes were plotted and analyzed
281 using Dunn's multiple comparisons.
282
283 **Immunohistochemistry**
284 Larvae were fixed with 4% PFA, dehydrated with Methanol, rehydrated using a graded series of
285 PBSDT (1x PBS with 0.25% Tween-20 and 1% DMSO): Methanol and then treated with 150
286 mM Tris-HCl for antigen retrieval. Samples were then washed and permeabilized with ice cold
287 100% acetone, followed by more washes. Samples were blocked for 2 hours at room
288 temperature with 6% goat serum and 3% BSA, then incubated overnight with 1:1000 anti-
289 acetylated tubulin rabbit primary antibodies (ThermoFisher). Samples were then incubated
290 overnight with 1:1000 anti-rabbit Alexa 488 (Invitrogen) secondary antibodies, protected from
291 light.
292
293 **Lysotracker**
294 5 dpf PTU-treated larvae were sorted and placed in mutant-sibling pairs in a 2 mL Eppendorf
295 tube. LysoTracker Red DND-99 (Invitrogen) was diluted to 1:100 to examine brains or 1:200 to
296 examine inner ear hair cells. Larvae were incubated in Lysotracker for 40 minutes at 28.5°C
297 with the tube left open but protected from light. The larvae were then washed with E3 buffer for
298 10 minutes and immediately imaged.
299 Hindbrain lysotracker uptake was quantified by selecting a single Z-stack slice of the
300 hindbrain region and thresholding it to highlight particles in the size range of endosomal

301 compartments (size = 0.02-2 μm). The integrated density and area of particles from two equally
302 sized regions of interest from hindbrain sections and a single region of neuropil were measured
303 from each slice using the Analyze Particles function of ImageJ. The integrated density
304 measurements were averaged and normalized to the integrated density of the neuropil.
305
306 **CD63-phluorin Injections and Analysis**
307 pUbi-CD63-pHluorin was a gift from Frederik Verweij and was generated as described in
308 (Verweij et al., 2019). Nacre-background *vps4a*^{T248I} mutant and sibling embryos were injected
309 at the one cell stage with 100 ng/μL pUbi-CD63-pHluorin. Damaged embryos were sorted out,
310 and only larvae with CD63-pHluorin expression on muscle cell membranes were selected for
311 live imaging on 3-4 dpf. Time lapse videos were recorded at 50 fps for 2 minutes at 63x with a
312 2x optical zoom. For analysis, three frames were combined, and the mean pixel intensity was
313 measured from regions of the ventricular intracranial space, surrounding tissue as background,
314 and muscle cells. The mean pixel intensity of ventricular intracranial space was normalized to
315 background and then divided by muscle cell pixel intensity.
316
317 **Bulk Tissue RNASeq**
318 Total RNA was isolated from 5 dpf wild type and vps4a mutant larvae (n = 15-20 each
319 genotype) using TRIzol reagent (Thermo Fisher, 15596026) according to the manufacturer's
320 protocol. RNA-seq library construction and single-end sequencing were performed by the OHSU
321 Massively Parallel Sequencing Shared Resource (RRID SCR_009984, Oregon Health &
322 Science University, Portland, OR, USA). Sequencing reads were mapped to the Danio rerio
323 GRCz10 genome using Tophat v2.1.1 (Kim et al., 2013) from within an OSHU instance of the
324 Galaxy sequence analysis platform (Afgan et al., 2016). The resulting BAM files were imported
325 to SeqMonk v1.42.0 (www.bioinformatics.babraham.ac.uk/projects/seqmonk/) for data

326 visualization and statistical analysis using the Intensity Difference filter for unreplicated data
327 sets. Genes with an adjusted p-value < 0.05 were considered differentially expressed.
328
329 **Hybridization Chain Reaction (HCR)**
330 For HCR, custom probes for *vps4a*, *atf3*, *jun*, *gap43, opn1sw1* and the corresponding
331 fluorescent B-amplifier hairpins were ordered from Molecular Instruments
332 (https://www.molecularinstruments.com/). Probes were chosen based on their log2(fold
333 change) and number of reads from bulk RNA sequencing analysis. Probes were assigned B-
334 amplifiers with the intention of doing multi-plex experiments. Probe sequences are considered
335 confidential and proprietary information of Molecular Instruments based on their Terms and
336 Conditions, so further inquiries may be directed to their technical team.
337 PTU-treated larvae were sorted at 5 dpf and fixed overnight in 4% paraformaldehyde
338 (PFA) at 4°C with rocking. After fixation, larvae were washed in PBST (1X PBS with 0.1%
339 Tween-20), dehydrated with a methanol:PBS series (25%, 50% and 75% methanol in PBS),
340 then stored at least overnight at -20°C. Larvae were subsequently rehydrated with a reverse
341 methanol:PBST series, washed several times with PBST, permeabilized for 15 minutes with 20
342 µg/mL Proteinase K, post-fixed with 4% PFA and then washed again. Probe detection and
343 amplification with fluorescent hairpins was performed as recommended by the MI protocol for
344 whole mount zebrafish larva with extended pre-hybridization and pre-amplification times (4
345 hours each) and probe concentrations adjusted based on the reads of each probe (2 nM for *atf3*
346 and *jun*, 5 nM for *gap43*, 10 nM for *vps4a*).
347
348 **Calcium Imaging**
349 Larvae at 3 dpf *vps4a*^{T248I} *Tg(α-tubulin-gal4:UAS-GCaMP7a)* were sorted for strong GCaMP
350 expression in the brain. 5 dpf GCaMP positive larvae were mounted in 2% low melt agarose on

351 a custom depression slide fitted with a mini-speaker (DAEX-9-45M Skinny Mini Exciter 9 mm 1
352 W 4 Ohm). Using an AIYIMA A07 amplifier, tone stimuli were played through the mini speaker
353 using a custom script in MATLAB (R2020b, MathWorks). 600 Hz (0.35 V) or 450 Hz (0.2 V)
354 tones were played for 0.6 seconds or 0.1 seconds, respectively, five times with 10 second
355 intervals. Time lapse images and fluorescence values were recorded using LAS-X software
356 (Ver 3.7.2.22383). To account for variability in GCaMP7a expression between larvae, all
357 fluorescence values were normalized by subtracting background measurements. Traces were
358 generated by averaging the normalized fluorescence value (F) for each time point across all
359 larvae and plotting this value over time. To calculate percentage change in fluorescence
360 (ΔFt/F0%), 2-3 frames, containing image artifacts (due to the tone stimulation shaking the slide)
361 were identified for each stimulus, and fluorescence values corresponding to these frames were
362 discarded. The F0 measurement was selected from the frame prior to tone stimulation, based
363 on the time lapse video and presence of artifact frames, and Ft was selected as the highest
364 frame immediately after tone stimulation. (ΔFt/F0)/F0 was used to calculate the change in
365 GCaMP7a fluorescence and was multiplied by 100 to convert into a percentage to generate
366 "(ΔFt/F0%)". The average percentage change in fluorescence was then calculated for each
367 larva and differences between wild-type siblings and *vps4a* mutants was analyzed using
368 unpaired t tests.
369
370 **Retrograde Labeling of Mauthner Cells**
371 Retrograde labeling was adapted from previously published methods (Gahtan et al., 2002;
372 Wehner et al., 2017). Larvae were anesthetized with 0.3% MESAB prior to spinal injection of 10
373 mg/mL 10,000 MW Tetramethylrhodamine dextran (10,000 MW, D1866, Thermo Fisher) in
374 PBS. Custom glass injection needles were prepared from borosilicate glass capillaries
375 (TW100F-4, World Precision Instruments) using a micro-needle puller (Suttner Instruments Co,
376 Model P-87) using heat cycle 517, pulling cycle 75, velocity 75 and time 90, and then the tip was

377 broken using forceps. Larvae were mounted laterally in 2% low melt agarose for injection, and
378 then incubated in E3 media overnight to recover before imaging.
379
380 **Microscopy and Image Processing**
381 Images for LysoTracker, CD63pHluorin, and HCR were take using an upright LSM700 laser-
382 scanning confocal microscope with Zeiss Zen software (Carl Zeiss). For live imaging of larva,
383 they were anesthetized in 0.03% MESAB in E3 media and mounted in 2% prewarmed low melt
384 agarose. Images were collected using 488 nm, 555 nm and 647 nm lasers, depending on the
385 requirements of the individual experiment (Acetylated Tubulin and CD63pHluorin used 488 nm,
386 LysoTracker used 555 nm, HCR used up to all three depending on the fluorescent hairpins
387 used). We used a Leica HC PL Fluotar 10x/0.3 lens for Acetylated Tubulin, HCR and
388 LysoTracker images, a Plan Apochromat 40x/1.0DIC lens for LysoTracker quantification images
389 and an Acroplan 63x/0.95W water immersion lens for higher magnification HCR images. Laser
390 power and gain were determined independently for each fluorophore and kept consistent within
391 each experiment. The FIJI build of ImageJ Version 2.1.0/1.53t was used to process all raw
392 image files. For Calcium Signaling, scans were taken using a Leica SP-8 Confocal Microscope
393 equipped with a 20x (NA 1.0) objective, using LAS-X software. Images were collected using
394 488 nm white laser light.
395
396 **Experimental Design and Statistical Analysis**
397 The number of zebrafish larvae used is denoted in the figure legends. G*Power software was
398 used to ensure there were sufficient samples tested. All statistical analyses were performed
399 using GraphPad Prism software (version 9). The data was tested for normal distribution using
400 Shapiro-Wilk test. Data is presented as mean ± SD, and significance between mutant and wild-
401 type sibling groups was determined using unpaired t test unless otherwise noted. The image in

402 figure 1C was adapted from Sun et al., 2017 using Mol* (Sehnal et al., 2021) and RCSB PDB
403 (PDB ID:5XMI) software.
404
405
406 **Results**
407 **A missense mutation in *vps4a* reduces ATPase activity and ESCRT-III filament**
408 **disassembly**
409 *raumschiff* mutants were generated from an ENU mutagenesis screen for genes that affect
410 larval auditory and vestibular function (Haffter et al., 1996). Mutant larvae fail to respond to
411 auditory cues and maintain an upright posture. The mutation is recessive and fully penetrant at
412 5 days postfertilization (dpf) with lethality occurring around 9-10 dpf. To identify the causative
413 gene of the *raumschiff* phenotype, we used whole-genome sequencing and identified a
414 threonine to isoleucine missense mutation in *vps4a* using SNPTrack (Leshchiner et al., 2012).
415 The critical interval for *raumschiff* was also mapped to a region approximately 700 kb (or 1 cM)
416 south of the polymorphic marker z5669, placing the locus at 34.33 Mb on Chromosome 25.
417 *vps4a* is located at 34.93Mb on Chromosome 25, which is within the predicted region for the
418 causative gene. No other polymorphisms were identified by SNPTrack in this region (Fig. 1A).
419 Vps4a is a hexameric type I AAA-ATPase member of the ESCRT-III complex, whose
420 role is to promote the dissociation of the ESCRT-III subunits via ATP hydrolysis (Babst et al.,
421 1997; Davies et al., 2010; Monroe et al., 2014; McCullough et al., 2018). The threonine to
422 isoleucine mutation (T248I) we identified is present in the AAA ATPase domain in a region that
423 is highly conserved between species (Fig. 1B). To determine whether the T248I mutation was
424 comparable to a nonsense allele of *vps4a*, we edited the *vps4a* locus using multiple
425 CRISPR/Cas9 guides (Wu et al., 2018; Kroll et al., 2021). In our experiments, multi-guide
426 injections resulted in a G0 phenotype in 16.9% of injected larvae that was indistinguishable from
427 the auditory/vestibular phenotype observed in *vps4a*^{T248I} mutants (400 embryos were injected at

428 < 1 hour past fertilization; of the larvae that survived to 5 dpf, 56/331 larvae showed absence of
429 acoustic startle reflexes and abnormal posture). These results suggest that the T248I mutation
430 is comparable to a null allele of Vps4a. In addition, the *vps4b* paralogue is also ubiquitously
431 expressed (Yang et al., 2016), therefore we generated *vps4a/vps4b* G0 double mutants using
432 CRISPR-based editing to test whether *vps4b* could compensate for the loss of *vps4a* during
433 development. A previous study using morpholinos against *vps4b* reported a tooth phenotype
434 analogous to human dentin dysplasia I (Yang et al., 2016). We observed that embryos injected
435 with multiple CRISPR guides against *vps4b* alone, or *vps4a* and *vps4b* together, developed
436 normally until 3 dpf. The lack of embryonic lethality is presumably due to the presence of
437 maternal RNA during early developmental stages. However, in contrast to the morpholino study,
438 *vps4b* and *vps4a/4b* multi-guide injected larvae exhibited progressive necrosis and by 5 dpf,
439 there was complete lethality (558 embryos were injected with *vps4b* guides; 468 larvae survived
440 to 1 dpf, and 2 survived to 5 dpf. 298 embryos were injected with *vps4a/4b* guides; 236 larvae
441 survived to 1 dpf, and 1 survived to 5 dpf). Our results suggest that *vps4b* is required for global
442 cellular homeostasis whereas *vps4a* selectively affects the nervous system. A similar effect was
443 reported for the Nsfa and Nsfb AAA-ATPases that mediate vesicle fusion; mutations in zebrafish
444 *nsfa* largely affect the nervous system, while the loss of *nsfb* functions leads to general necrosis
445 at 4 dpf (Woods et al., 2006; Hanovice et al., 2015; Gao et al., 2023).
446 Based on the Cryo-EM structure of the yeast Vps4 AAA-ATPase (Sun et al., 2017),
447 threonine 248 is located at the interface between Vps4a hexamer subunits (Fig. 1C). To assess
448 the effect of the isoleucine substitution on ATPase activity, we generated an equivalent
449 mutation, T254I, in the AAA ATPase domain of yeast Vps4. When tested for ATPase activity *in*
450 *vitro*, $Vps4^{T254I}$ had severely reduced enzymatic activity compared to wild-type Vps4a, although
451 some activity remained ($p < 0.0001$, $n_{WT} = 4$, $n_{vps4(T254I)} = 4$, $t = 47.92$, df = 6) (Fig. 1D).
452 To determine whether the residual function of the T254I protein could mediate filament
453 disassembly, we incubated $Vps4^{T254I}$ with the ESCRT-III filaments formed by Vps2, Vps24 and

454 Snf7 *in vitro* and used sedimentation to assess disassembly. In our assay, disassembled
455 ESCRT-III filament proteins are present in the supernatant whereas assembled filaments
456 sediment to the pellet fraction (Sun et al., 2017). We observed that wild-type Vps4a completely
457 disassembled the ESCRT-III filaments, with all proteins found in the supernatant (Fig. 1E). In
458 contrast, mutant Vps4^{T254I} only partially disassembled the ESCRT filaments (Fig. 1E). Using
459 negative stain electron microscopy (EM), assembled ESCRT-III filaments appear as rings or
460 have corkscrew structures (Fig. 1F, upper left panel). When incubated with wild-type Vps4,
461 filament structures were absent, indicating full disassembly (Fig. 1F, upper right panel). In the
462 presence of Vps4^{T254I}, assembled filaments were still detectable albeit there were fewer
463 filaments compared to samples where no Vps4 protein was added (Fig. 1F, lower panels).
464 These results demonstrate that the T245I mutation at the interface between Vps4a subunits
465 reduces but does not fully abolish the ATPase activity of the protein, and this reduction in
466 activity is reflected in the incomplete disassociation of ESCRT-III filaments.
467

468 **The *vps4a^{T248I}* mutation results in enlarged endosomal membrane compartments and a**
469 **reduction of circulating exosomes in the CNS**

470 Using RNA-FISH, we found that the expression of *vps4a* transcripts is ubiquitous at 5 dpf, with
471 higher levels expressed in the CNS and retina (Fig. 2A). In light of the higher expression of
472 *vps4a* in the CNS and the neurological disorder in human patients, we focused our attention on
473 the larval brain. As stated previously, Vps4a mediates the formation of multivesicular bodies
474 from late endosomes. To determine if the mutation affects this function in the nervous system,
475 we performed *in vivo* imaging of LysoTracker, a vital dye that accumulates in acidic membrane
476 compartments such as low pH endosomal compartments. As shown in Fig. 2B, endocytic
477 compartments in *vps4a^{T248I}* mutants labeled more brightly with LysoTracker compared to wild-
478 type siblings. The average size and pixel density of acidic membrane compartments in the
479 hindbrain were quantified and we found that *vps4a^{T248I}* mutants have significantly larger acidic

480 membrane compartments (p = 0.0015, n_{WT} = 7, $n_{vps4a(T248I)}$ = 10, t = 3.873, df = 15) (Fig. 2C, left
481 panel) that take up more dye (p = 0.0020, n_{WT} = 7, $n_{vps4a(T248I)}$ = 10, t = 3.744, df = 15) (Fig. 2C,
482 right panel). Together, these results imply that the *vps4a*^{T248I} mutation has a detrimental effect
483 on endocytic compartment processing in the CNS.

484 Given the known role of Vps4a in multivesicular body formation, we examined whether
485 the mutation affects the number of exosomes that are released upon fusion of multivesicular
486 bodies to the plasma membrane. To detect circulating exosomes in live fish, we used CD63-
487 pHluorin, a pH-sensitive GFP reporter that is quenched in intraluminal vesicles in low pH
488 multivesicular bodies and fluoresces when these vesicles are released into a higher pH
489 extracellular milieu as exosomes (Verweij et al., 2018). We microinjected a plasmid for
490 ubiquitous expression of CD63-pHluorin into single-cell stage embryos, and selected for larvae
491 that transiently expressed the CD63-pHluorin based on signal in the muscle cells, which is
492 readily detectable by 3 dpf (Fig. 2D). The plasma membrane of muscle cells was commonly
493 labeled in our injected fish as was previously reported (Verweij et al., 2018) and served as a
494 positive control for expression. We detected a strong reduction in CD63-phluorin signal in the
495 CNS blood vessels on 3 dpf (Fig. 2E), as well as in the midbrain ventricle of 4 dpf *vps4a*^{T248I}
496 mutants (Figs. 2F,G). We quantified the CD63-pHluorin signal in the midbrain ventricle and
497 normalized to background signal from the surrounding CNS tissue. The relationship between
498 CD63-pHluorin signal in the midbrain ventricle is moderately correlated to signal in the muscle
499 cells in wild-type siblings but not in mutants (Fig. 2H). We then calculated a ratio of the
500 normalized pixel intensity of the midbrain ventricle CD63-pHluorin signal to the muscle cell
501 CD63-pHlourin signal and found that the ventricle/muscle cell intensity ratio is significantly
502 decreased in *vps4a*^{T248I} mutants compared to wild-type siblings (p = 0.0382 (exact), n_{WT} = 16,
503 $n_{vps4a(T248I)}$ = 8, Mann-Whitney test) (Fig. 2I). This result indicates that there is a decrease in the
504 number of exosomes present in the brain ventricle of mutants, supporting the hypothesis that
505 biogenesis of these extracellular vesicles is reduced by the *vps4a*^{T248I} mutation.

506

507 **Transcriptional changes in the *vps4a*^{T248I} mutant**

508 Considering the broad changes in endosomal morphology and the reduction in circulating
509 exosomes in the CNS of *vps4a*^{T248I} mutants, we next examined the gross morphology of the
510 brain. Using whole mount immunohistochemistry, we labelled the axonal fibers of mutants and
511 siblings with acetylated tubulin antibody to visualize axon morphology. No obvious changes in
512 gross morphology between wild-type siblings and *vps4a*^{T248I} mutants were apparent (Fig. 3A).
513 The lack of obvious developmental defects is likely due to the presence of maternal mRNA.
514 However, we noted the presence of pyknotic nuclei (Fig. 3B), which are associated with cell
515 death (Hou et al., 2016). We quantified the number of these abnormal cells and found that
516 *vps4a*^{T248I} mutants have significantly more abnormal cells in the CNS compared to wild-type
517 siblings and that cell death increases during development (5 dpf, $p < 0.0001$ (exact), $n_{WT} = 12$,
518 $n_{vps4a(T248I)} = 14$, Mann-Whitney Test; 7 dpf, $p < 0.0002$ (exact), $n_{WT} = 8$, $n_{vps4a(T248I)} = 7$, Mann-
519 Whitney Test).

520 As exosomes carry cargo containing microRNA and DNA and have been implicated in
521 the regulation of DNA transcription (Kalluri and LeBleu, 2020), we assayed for transcriptional
522 changes in the *vps4a*^{T248I} mutant by performing a differential gene expression analysis on a bulk
523 RNAseq data set that was initially used to find the mutation. We then used HCR RNA-FISH to
524 validate the top $\log_2$ fold changes in gene expression. We found that the immediate early
525 response genes *atf3* and *jun,* and the axonal regeneration gene *gap43* were dramatically
526 upregulated in mid- and hindbrain regions in the *vps4a*^{T248I} larvae (Fig. 3C, D). These striking
527 changes in gene expression are consistent with a failure in intercellular communication by
528 exosomes, and/or endosomal processing within neurons.

529

530 **Impaired vision in *vps4a*^{T248I} mutants**

531 The clinical profile of human patients with missense mutations in *VPS4A* includes visual deficits
532 with a range of symptoms such as retinal dystrophy and cataract formation (Rodger et al., 2020;
533 Seu et al., 2020). Although we did not observe expanded melanophores in the *vps4a*^{T248I}
534 mutant, which are indicative of blindness in larvae, we did find pronounced changes in visual
535 function and gene expression in the retina. The optomotor response (OMR) in zebrafish is a
536 reflex that can be evoked by a visual stimulus such as moving stripes, which causes the fish to
537 swim in the direction of perceived motion, resulting in stabilization relative to the environment
538 (Kist and Portugues, 2019). Compared to wild-type siblings, *vps4a*^{T248I} mutant larvae have a
539 greatly reduced OMR, suggesting they are blind ($p < 0.0001$ (exact), $n_{WT} = 12$, $n_{vps4a(T248I)} = 10$,
540 Mann-Whitney test) (Fig. 4A). To investigate this defect further, we recorded electroretinograms
541 (ERG) to assess the light induced changes in the electrical potential of the whole retina. The b-
542 wave amplitude generated from an ERG can provide insight into the function of the outer retina
543 (Niklaus et al., 2017). A range of light intensities (from the dimmest at log-4, to the brightest at
544 log0) were tested and we found that the b-wave amplitude in *vps4a*^{T248I} mutants is significantly
545 decreased compared to wild-type siblings (log 0, $p < 0.0001$, $n_{WT} = 23$, $n_{vps4a(T248I)} = 34$; log -1, p
546 < 0.0001, $n_{WT} = 23$, $n_{vps4a(T248I)} = 33$; log -2, $p < 0.0001$, $n_{WT} = 23$, $n_{vps4a(T248I)} = 34$; log -3, $p =$
547 0.0014, $n_{WT} = 23$, $n_{vps4a(T248I)} = 34$; log -4, $p = 0.1989$, $n_{WT} = 23$, $n_{vps4a(T248I)} = 34$, Kruskal-Wallis
548 test) (Fig. 4B). In addition, we found that *jun* and *gap43* are upregulated in the retina of
549 *vps4a*^{T248I} mutants, specifically in the photoreceptor and retinal ganglion layers (Fig. 4C). We
550 also detected reduced *opn1sw1* expression in the photoreceptors of mutants. Together, these
551 analyses indicate that the *vps4a*^{T248I} mutants have pronounced visual defects originating in the
552 retina. Notably, the decrease in b-wave amplitude is variable among individual mutants and
553 may not fully explain the absence of the OMR.
554
555 **Selective vestibular defects in *vps4a*^{T248I} mutants**

556 At the free-swimming stage of development (5 dpf), *vps4a*^{T248I} larvae do not maintain an upright
557 posture, swim sideways or upside down, and do not inflate their swim bladder, which is
558 classically associated with functional deficits in vestibular hair-cells (Nicolson, 2017). To further
559 investigate this phenotype in *vps4a*^{T248I} mutant larvae, we tested vestibular function by
560 assessing vestibular induced eye movements (VIEM) (Mo et al., 2010). Larvae with loss of hair-
561 cell function mutations have reduced eye movements in response to head rotation (Nicolson,
562 2017), however, we did not observe a significant difference between the *vps4a*^{T248I} mutants and
563 wild-type siblings (p = 0.4632 (exact), n_{WT} = 18, $n_{vps4a(T248I)}$ = 16, Mann-Whitney test) (Fig. 5A).
564 As mutant larvae have pronounced postural defects, we also tested the vestibulospinal reflex
565 (VSR), which assesses vestibular induced motor function in the trunk (Gao and Nicolson, 2021).
566 We compared the maximum tail angle between wild-type siblings and mutants and found the
567 *vps4a*^{T248I} mutants had a significantly reduced tail angle (p = 0.0012 (exact), n_{WT} = 7, $n_{vps4a(T248I)}$
568 = 10, Mann-Whitney test) (Fig. 5B). The normal VIEM along with the reduced VSR result
569 suggests that *vps4a*^{T248I} mutants have selective defects in vestibular pathways.
570 In zebrafish, acceleration of the head is detected by utricular hair cells (Tanimoto et al.,
571 2009; Mo et al., 2010; Sun et al., 2018), which then transmit signals to the utricular afferents of
572 the VIIIth cranial nerve (Fig. 5C). The VIIIth nerve innervates the superior vestibular nucleus
573 (SVN), vestibulospinal cell (VS) and tangential nucleus (TAN), as well as the Mauthner cell in
574 the hindbrain (Bianco et al., 2012; Jia and Bagnall, 2022; Liu et al., 2022; Hamling et al.,
575 2023b). Signals from the SVN and TAN are relayed by the oculomotor and trochlear nuclei to
576 oculomotor muscles to produce eye movements associated with the VIEM (Fig. 5C;(Bianco et
577 al., 2012; Liu et al., 2022; Sugioka et al., 2023)). VS neurons directly innervate motor neurons
578 in the trunk to produce tail movements (Liu et al., 2022; Sugioka et al., 2023). To assess the
579 function of the VSR circuit, we used a pan-neuronal GCaMP7a calcium indicator to visualize
580 neuronal activity (Muto et al., 2013). Recently it was demonstrated that utricular hair cells in
581 zebrafish larvae respond to high frequency tones, analogous to the responses of vestibular hair

582 cells to bone-conducted vibration in mammals (Privat et al., 2019; Tanimoto et al., 2022). To
583 stimulate the vestibular circuitry mediating the VIEM and VSR, we delivered pulses of 600 Hz at
584 110 dB using a mini-speaker attached to the glass slide on which larvae were mounted for
585 calcium imaging. Electron microscopy data has shown that the lateral dendrite of the Mauthner
586 cell is adjacent to the VS nucleus (Liu et al., 2022). To visualize this dendrite, we performed
587 backfill injections of rhodamine dextran prior to calcium imaging, enabling us to use the
588 Mauthner cell as a landmark for the approximate locations of the SVN, VS and TAN (Fig. 5D).
589 Upon tone stimulation, neurons in all three nuclei responded with an increase in fluorescence
590 (Fig. 5D'). Nevertheless, the average raw fluorescence trace for the VS region has a slightly
591 lower peak amplitude in the *vps4a*^{T248I} mutant compared to wild-type siblings (Fig. 5E, right).
592 Analysis of the group data from individual fish indicates that the percentage change in
593 normalized fluorescence in the VS region is reduced in *vps4a*^{T248I} mutants (p = 0.0337 (exact),
594 n_{WT} = 11, $n_{vps4a(T248I)}$ = 15, t = 2.252, df = 24)(Fig. 5F, right). As predicted by our behavioral
595 analysis, we did not observe a significant difference in the raw fluorescence trace or percentage
596 change in normalized fluorescence in the TAN or SVN between *vps4a*^{T248I} mutants and wild-
597 type siblings (TAN p = 0.6224 (exact), SVN p = 0.1405 (exact), n_{WT} = 11, $n_{vps4a(T248I)}$ = 15, t =
598 0.4988 (SVN), df = 24 (SVN), t = 1.524 (TAN), df = 24 (TAN)) (Figs. 5E,F, left and center).
599 Overall, our calcium imaging data confirm that the VIEM circuit is intact and suggest that
600 reduced activity in the VS neurons, which directly innervate motor neurons, contributes in part to
601 the reduction in tail movements in response to vestibular cues in the *vps4a*^{T248I} mutants.
602

603 **Intact ascending auditory pathway in *vps4a*^{T248I} mutants**

604 In zebrafish, auditory signals excite saccular hair cells, which are innervated by the afferent
605 neurons of the statoacoustic ganglion (or VIIIth nerve). If the auditory cues are sufficiently loud
606 enough to startle, the signal is transmitted to the giant escape fiber neuron known as the

607 Mauthner cell, which directly activates motor neurons (Kohashi and Oda, 2008; Sillar, 2009;
608 López-Schier, 2019). Less intense sounds activate hindbrain neurons within the medial
609 octavolateralis nuclei region, which then communicate with the torus semicircularis for further
610 auditory processing (Echteler, 1984; Tanimoto et al., 2009; Inoue et al., 2013; Vanwalleghem et
611 al., 2017) (Fig. 6A). *vps4a*^{T248I} mutant larvae are largely unresponsive to tapping on the petri
612 dish, suggesting that hearing is profoundly impaired. We assessed the severity of this defect by
613 quantifying the auditory evoked behavioral response (AEBR), which is a startle response to
614 loud, pure tone stimuli. *vps4a*^{T248I} mutant larvae responded to pure tones significantly less
615 compared to wild-type siblings, indicating that mutants have pronounced defects ($p < 0.0001$
616 (exact), $n_{WT} = 15$, $n_{vps4a(T248I)} = 20$, Mann-Whitney test) (Fig. 6B). The pan-neuronal GCaMP7a
617 calcium indicator was used to examine neuronal activity in the saccular hair cells and
618 statoacoustic ganglion in response to the same 110 dB 600 Hz stimulus (Figs. 6C,D). In
619 saccular hair cells, we observed robust responses in average raw fluorescence traces (Fig. 6E)
620 and comparable calcium transients in wild-type or mutant individual fish ($p = 0.4162$ (exact), n_{WT}
621 $= 20$, $n_{vps4a(T248I)} = 13$, $t = 0.8228$, df = 35) (Fig. 6F). Comparable responses were also seen in
622 the statoacoustic ganglion ($p = 0.8748$ (exact), $n_{WT} = 20$, $n_{vps4a(T248I)} = 13$, $t = 0.1588$, df = 31)
623 (Figs. 6E,F). These results are consistent with LysoTracker labeling, which shows no significant
624 difference in dye uptake between wild-type siblings and *vps4a*^{T248I} mutant in hair cells in the
625 saccule ($p = 0.0934$ (exact), $n_{WT} = 6$, $n_{vps4a(T248I)} = 9$, $t = 1.810$, df = 13), utricle ($p = 0.6314$
626 (exact), $n_{WT} = 6$, $n_{vps4a(T248I)} = 9$, $t = 0.4913$, df = 13) or anterior cristae ($p = 0.3233$ (exact), $n_{WT} =$
627 10, $n_{vps4a(T248I)} = 10$, $t = 1.016$, df = 18).
628 The auditory circuitry within the hindbrain for non-startle responses is less well defined
629 in larvae, therefore we focused on a midbrain region of the ascending auditory pathway and
630 examined neuronal activity in the torus semicircularis, which is akin to the inferior colliculus in
631 mammals and key for auditory processing (McCormick, 1999; Edds-Walton and Fay, 2008;
632 Vanwalleghem et al., 2017). This midbrain structure is located beneath the optic tectum at the

633 level of the semicircular canals and saccule of the inner ear and the medial longitudinal
634 fasciculus (MLF) (Fig. 6G). We observed a visible increase in GCaMP7a reporter activity in the
635 torus semicircularis of both wild-type siblings and *vps4a*^{T248I} mutants after pure tone stimulation
636 (Fig. 6H). No significant differences were detected in the average raw fluorescence traces or
637 percentage change in normalized fluorescence between wild-type siblings and *vps4a*^{T248I}
638 mutants for the torus semicircularis (p = 0.9672 (exact), n_{WT} = 11, $n_{vps4a(T248I)}$ = 13, t = 0.04157,
639 df = 22) (Figs. 6I,J). Together, these data indicate that the ascending auditory pathway of
640 *vps4a*^{T248I} mutants including the inner ear and central circuitry is functional.
641

642 **Defective sensorimotor transformation in *vps4a*^{T248I} mutants**

643 Although *vps4a*^{T248I} mutants have a greatly reduced acoustic startle response, our data
644 demonstrate that auditory cues activate the ascending auditory pathway. Notably, mutant larvae
645 are not paralyzed, however, they are largely inactive at the free-swimming stage. Therefore, we
646 assessed whether *vps4a*^{T248I} mutants have a general motor system defect that prevents motor
647 responses to sensory cues.

648 To test whether startle reflexes are globally affected, we measured the ability of
649 *vps4a*^{T248I} mutants to produce a deep C-bend of the trunk in response to contact of a stiff probe
650 with the dorsal region of the head. We observed that both wild-type siblings and *vps4a*^{T248I}
651 mutants displayed robust C-bend motions of their trunks in response to touch (Figs. 7A,B; p =
652 0.1079 (exact), n_{WT} = 10, $n_{vps4a(T248I)}$ = 11, t = 1.687, df = 19). This result suggests that touch
653 receptors, along with Mauthner cells and other vital components of motor output such as spinal
654 cord neurons, motor neurons, and muscle cells are functional. In addition, axonal fibers in
655 superficial layers of the skin, the hindbrain, and anterior trunk regions did not show any changes
656 in gross morphology in *vps4a*^{T248I} mutants (Fig. 7C). These data point to a deficit within central

657 circuitry in *vps4a*^{T248I} mutants as downstream motor components of the startle reflex are
658 unaffected.

659 As described above, auditory signals from the statoacoustic ganglion are directly
660 transmitted to the Mauthner cell, which innervates trunk motor neurons to generate an escape
661 reflex. However, the 110 dB intensity of our tone stimulus did not result in detectable activation
662 of the Mauthner cell soma, which is consistent with a previous imaging study (Marsden and
663 Granato, 2015). Instead, we observed a reliable response in the midbrain nucleus of the medial
664 longitudinal fasciculus (nMLF) (Figs. 7D, E-H). The nMLF is a vital component of the
665 descending motor system, serving as a command center for forward locomotion (Sankrithi and
666 O'Malley, 2010; Koyama et al., 2011; Severi et al., 2014; Thiele et al., 2014; Wang and McLean,
667 2014; Migault et al., 2018; Shimazaki et al., 2019; Xu et al., 2021). The nMLF contains
668 subpopulations of vGlut1 and vGlut2 positive neurons, which control both fast escape-swimming
669 behaviors as well as slow forward locomotion (Severi et al., 2014; Berg et al., 2023). Neurons
670 in the nMLF were recently shown to respond to hindbrain cranial relay neurons (CRN; Fig. 7D),
671 which can be activated by aversive auditory stimulation of Mauthner cells, leading to smooth
672 swimming after an initial C-bend response (Xu et al., 2021). Although the auditory circuitry to the
673 nMLF activated by non-startle stimuli has not been characterized, the nMLF has been
674 implicated in fine postural control via inputs from the TAN of the ascending vestibuloocular
675 pathway (Sugioka et al., 2023). Notably, activation of neurons in the TAN in *vps4a*^{T248I} mutants
676 is comparable to wild-type responses.

677 Considering that the nMLF is central to motor function in response to sensory cues, we
678 compared GCaMP7a signals in this cluster of neurons between wild-type siblings and *vps4a*^{T248I}
679 mutants in response to the 600 Hz stimulus. These midbrain clusters can be identified based on
680 their prominent axonal tracts that descend near the midline (Fig. 7E). We found that the peak
681 amplitudes of calcium transients in the average raw fluorescence trace in the mutant were
682 markedly decreased (Figs. 7F-G). In addition, the percentage change in normalized

683 fluorescence in the nMLF was significantly reduced in all individual *vps4a*^{T248I} mutants tested (p
684 < 0.0001 (exact), $n_{WT} = 14$, $n_{vps4a(T248I)} = 11$, $t = 6.937$, df = 23) (Fig. 7H).
685 We next investigated the neuronal activity of the spinal cord in response to tone
686 stimulation using the pan neuronal GCaMP7a reporter (Fig. 7I). The average raw fluorescence
687 trace of the *vps4a*^{T248I} mutants show lower peaks in response to tone stimulation (Fig. 7K). In
688 the examples shown in Figure 8J, a second reporter (GCaMP7a expressed under a muscle cell
689 promoter, (Leung et al., 2019)) in the trunk muscles shows activation in the wild-type larva but
690 none in the mutant. Overall, the percentage change in normalized fluorescence is strongly
691 reduced in *vps4a*^{T248I} mutants ($p < 0.0001$ (exact), $n_{WT} = 11$, $n_{vps4a(T248I)} = 9$, Mann-Whitney test)
692 (Fig. 7L). Together, our results indicate that tone stimulation fails to trigger responses in the
693 nMLF descending motor pathway and downstream trunk motor neurons in *vps4a*^{T248I} mutants.
694
695
696 **Discussion**
697 Our study identifies a role for *vps4a* in sensorimotor transformation during larval development in
698 zebrafish. The T248I mutation in *vps4a,* which was isolated in a forward genetic screen for
699 balance and hearing deficits, profoundly affects enzymatic function, leading to defects in
700 ESCRT filament disassembly and membrane scission-dependent processes such as exosome
701 biogenesis. In *vps4a*^{T248I} larvae, we observe an increase in the expression of *jun* and *atf3* stress
702 response genes and a progressive loss in cellular homeostasis in the developing brain and
703 retina. Although identified as a deafness mutant, the function of the inner ear in *vps4a*^{T248I} larvae
704 is unaffected. Combined behavioral analyses and *in vivo* imaging of circuit activity demonstrate
705 that the ascending auditory pathway and descending motor pathways are intact in *vps4a*^{T248I}
706 mutants, however, mutants do not respond to aversive acoustic stimuli. These data suggest that
707 loss of *vps4a* function induces early onset of deficits in the transformation of sensory signals,
708 particularly auditory, vestibular, and visual input into motor responses.

709 **Defective disassembly of ESCRT filaments and decreased exosome biogenesis in**
710 **zebrafish *vps4a* mutants**

711 Our biochemical analyses indicate that the substitution of the corresponding threonine
712 residue with isoleucine in the ATPase domain of yeast *Vps4* strongly reduces ATPase activity
713 and ESCRT-III filament disassembly. *In vivo* imaging of the CNS revealed enlargement of acidic
714 compartments in larval mutants, which is consistent with previous studies in yeast *vps4* mutants
715 and human *VPS4A* patient fibroblasts (Bishop and Woodman, 2000; Frankel et al., 2017;
716 González et al., 2017; Willén et al., 2017). Enlarged endosomal compartments are likely due to
717 the disruption of endosomal processing and when membrane fails to invaginate and form
718 intraluminal vesicles via the ESCRT-mediated scission process. These vesicles can be released
719 from nearly all cell types as exosomes and contain a variety of signaling molecules, such as
720 proteins, lipids, and nucleic acids (Colombo et al., 2014; Zhang et al., 2019; Gurunathan et al.,
721 2021; Waqas et al., 2022). Exosomes have been implicated in a several diseases such as
722 cancers and neurodegenerative diseases due to the vital role they play in intercellular
723 communication (Lim and Lee, 2017; Bebelman et al., 2020; Dilsiz, 2020; Gomes et al., 2020;
724 Duarte-Silva et al., 2022; Han et al., 2023). A previous study on erythroid cells, which found
725 that transferrin receptor trafficking, a process dependent on proper endosomal sorting and
726 exosome secretion, is disrupted in human patients with *de novo VPS4A* mutations (Seu et al.,
727 2020). Here we show direct evidence for reduced exosome biogenesis using a CD63-pHluorin
728 marker of circulating exosomes. Both in blood vessels and brain ventricles, *vps4a*^{T248I} mutants
729 show a marked decrease in CD63-pHlourin signal. Disruptions to intercellular signaling through
730 exosomes can manifest as transcriptional changes (Dobrowolski and De Robertis, 2012; Budnik
731 et al., 2016; Gurung et al., 2021). We found that several genes associated with transcription
732 (*atf3* and *jun*), or regeneration (*gap43*) were highly upregulated in the CNS of *vps4a*^{T248I}
733 mutants. *atf3* and *jun* are known stress response genes, whereas upregulation of *gap43* may
734 be a compensatory response to disruption of axonal processes. Although exosomes mediate

735 cell-to-cell signaling and are important for cellular homeostasis, it is unclear whether the
736 transcriptional changes in *vps4a*^{T248I} mutants are due to (*i*) reduced exosome signaling, (*ii*)
737 disruptions in endosomal trafficking, or (*iii*) a combination of both defects. Alternatively, other
738 disruptions to membrane scission in the CNS may be involved as well. The expression of stress
739 response genes in the CNS in zebrafish mutants during larval development is consistent with
740 the microcephaly seen in human patients. While we did not observe changes in gross
741 morphology of the CNS, cell death in the brain was evident and increased during development.
742 We speculate that more pronounced defects would be evident in older animals, however, we
743 limited our analyses to early stages of larval development during which we could identify early
744 onset defects.
745
746 **Sensory and motor deficits**
747 Patients with *VPS4A* mutations are reported to have sensory deficits relating to vision
748 including retinal dystrophy and cataracts (Rodger et al., 2020). With respect to visual function in
749 *vps4a*^{T248I} mutants, larvae fail to swim in response to moving visual cues and outer retinal
750 responses to light are significantly reduced, signifying defects in vision that align with
751 transcriptional changes in the retina. The reduction in outer retinal function was variable among
752 mutants, whereas the optomotor response was severely reduced in all *vps4a*^{T248I} mutants,
753 suggesting that loss of photoreceptor function provides only a partial explanation of the absence
754 of vision-associated motor reflexes. Notably, human patients are reported to have difficulties in
755 fixing and following a moving object, which may be due to poor visual acuity or a combination of
756 poor vision and oculomotor pathway dysfunction.
757 Loss of central control of muscle tone, ataxia and motor delays are common traits found
758 in patients with neurodevelopmental disorders, including *VPS4A* patients (Rodger et al., 2020;
759 Seu et al., 2020). *vps4a*^{T248I} larvae share some of these features, such as lack of control over
760 posture and sensorimotor deficits. Vestibulospinal reflexes, which result in corrective

761 movements of the trunk, are greatly diminished in mutants. However, not all vestibular function
762 in lost; *vps4a*^{T248I} mutants still produce eye movements in response to rotation of the head.
763 Consistent with the behavioral data, neurons of the TAN and SVN, which are part of
764 vestibuloocular pathway (Bianco et al., 2012; Liu et al., 2022), show comparable activity in the
765 *vps4a*^{T248I} mutant to wild-type neurons. This data indicates that perturbation of Vps4a activity
766 does not result in global defects in vestibular function, or in brain function in general, but rather
767 that specific circuits are more sensitive to mutations in *vps4a*. Normal vestibular induced eye
768 movements and activation of TAN and SVN neurons also indicate that excitation of utricular hair
769 cells and vestibular afferent neurons is unaffected in *vps4a*^{T248I} mutants. In contrast to the
770 vestibuloocular pathway, the vestibulospinal circuit is impaired when *vps4a* is mutated.
771 Hindbrain VS neurons, which directly innervate trunk motor neurons, have decreased neuronal
772 activity in mutants. Recently it was shown that ablation of VS neurons leads to modest defects
773 in posture in zebrafish larvae (Hamling et al., 2023a), suggesting that other vestibular circuits
774 contribute to postural control. As such, the reduced activation of the vestibulospinal pathway in
775 *vps4a*^{T248I} mutants may only partially account for the inability to maintain an upright posture.
776 Further evidence for a loss in central control of motor responses emerged from our
777 analysis of the absence of an acoustic startle reflex in *vps4a*^{T248I} mutants. Despite the lack of
778 response to aversive acoustic stimuli, *vps4a*^{T248I} mutants have comparable activation of the
779 ascending auditory pathway as seen in wild-type siblings. Deficits in the descending motor
780 pathways or the spinal cord are also not the cause for the absence of the motor output in
781 response to visual or tone stimulation. *vps4a*^{T248I} mutants are not paralyzed and aversive touch
782 stimuli activate escape responses, demonstrating that mutant larvae can generate robust tail
783 movements. The above experiments indicate that both saccular afferent neurons and Mauthner
784 cells are activated by sound and touch in *vps4a*^{T248I} mutants, respectively, implying that a
785 second pathway may be defective in generating acoustic startle reflexes. One such pathway
786 may involve hindbrain spiral fiber neurons, which have been shown to be essential for Mauthner

787 cell-dependent escape responses (Lacoste et al., 2015). Nevertheless, our *in vivo* imaging
788 experiments using a non-startle tone stimulus revealed a pronounced reduction in the activity of
789 midbrain nMLF neurons and downstream spinal cord neurons of *vps4a*^{T248I} mutants. Neurons of
790 the nMLF play a key role in receiving sensory input and sending motor commands to the spinal
791 cord and are thought to play an analogous role to the interstitial nucleus of Cajal in the
792 mammalian midbrain, which controls eye and head movements (Fukushima, 1987; Severi et al.,
793 2014; Thiele et al., 2014). In zebrafish, both visual and vestibular systems provide sensory input
794 to the nMLF (Bianco et al., 2012; Matsuda and Kubo, 2021; Liu and Bagnall, 2023).
795 Interestingly, TAN neurons of the vestibuloocular pathway, also play a dual role of controlling
796 eye and body movements in zebrafish, and were recently shown to transmit signals about the
797 roll axis of the body to the nMLF, implicating this circuit in fine control of posture (Sugioka et al.,
798 2023). In *vps4a*^{T248I} mutants, TAN neurons are also activated by the tone stimulus, yet postural
799 defects are pronounced, further bolstering the notion that sensory input such as vestibular cues
800 fail to trigger sensorimotor transformation within the nMLF.
801
802 In summary, our combined biochemical and *in vivo* analyses have revealed that loss of
803 Vps4a function generates sensorimotor processing defects in the CNS of zebrafish larvae. Our
804 study provides a better understanding of the cause of motor dysfunction when *vps4a* is mutated.
805 Recent studies of exosome therapy for sensorimotor recovery after injury or resulting from acute
806 or chronic neurodegenerative disease (Chen et al., 2020; Yari et al., 2022; Zhang et al., 2023)
807 suggest that exosomes therapy may ameliorate the symptoms of neurodevelopmental disorders
808 such as those associated with *VPS4A*.
809
810
811
812

References

Afgan E et al. (2016) The Galaxy platform for accessible, reproducible and collaborative biomedical analyses: 2016 update. Nucleic Acids Res 44:W3–W10.

Alonso Y Adell M, Migliano SM, Teis D (2016) ESCRT-III and Vps4: a dynamic multipurpose tool for membrane budding and scission. FEBS J 283:3288–3302.

Babst M, Katzmann DJ, Estepa-Sabal EJ, Meerloo T, Emr SD (2002) Escrt-III: an endosome-associated heterooligomeric protein complex required for mvb sorting. Dev Cell 3:271–282.

Babst M, Sato TK, Banta LM, Emr SD (1997) Endosomal transport function in yeast requires a novel AAA-type ATPase, Vps4p. EMBO J 16:1820–1831.

Bebelman MP, Janssen E, Pegtel DM, Crudden C (2020) The forces driving cancer extracellular vesicle secretion. Neoplasia N Y N 23:149–157.

Berg EM, Mrowka L, Bertuzzi M, Madrid D, Picton LD, El Manira A (2023) Brainstem circuits encoding start, speed, and duration of swimming in adult zebrafish. Neuron 111:372-386.e4.

Beyer A, Scheuring S, Müller S, Mincheva A, Lichter P, Köhrer K (2003) Comparative sequence and expression analyses of four mammalian VPS4 genes. Gene 305:47–59.

Bianco IH, Ma L-H, Schoppik D, Robson DN, Orger MB, Beck JC, Li JM, Schier AF, Engert F, Baker R (2012) The Tangential Nucleus Controls a Gravito-inertial Vestibulo-ocular Reflex. Curr Biol 22:1285–1295.

Bishop N, Woodman P (2000) ATPase-defective Mammalian VPS4 Localizes to Aberrant Endosomes and Impairs Cholesterol Trafficking. Mol Biol Cell 11:227–239.

Budick SA, O'Malley DM (2000) Locomotor repertoire of the larval zebrafish: swimming, turning and prey capture. J Exp Biol 203:2565–2579.

Budnik V, Ruiz-Cañada C, Wendler F (2016) Extracellular vesicles round off communication in the nervous system. Nat Rev Neurosci 17:160–172.

Cacheiro P et al. (2020) Human and mouse essentiality screens as a resource for disease gene discovery. Nat Commun 11:655.

Cardoso AR, Lopes-Marques M, Silva RM, Serrano C, Amorim A, Prata MJ, Azevedo L (2019) Essential genetic findings in neurodevelopmental disorders. Hum Genomics 13:31.

843 Chen Y, Li J, Ma B, Li N, Wang S, Sun Z, Xue C, Han Q, Wei J, Zhao RC (2020) MSC-derived
844 exosomes promote recovery from traumatic brain injury via microglia/macrophages in
845 rat. Aging 12:18274–18296.

846 Cocucci E, Racchetti G, Meldolesi J (2009) Shedding microvesicles: artefacts no more. Trends
847 Cell Biol 19:43–51.

848 Colombo M, Raposo G, Théry C (2014) Biogenesis, Secretion, and Intercellular Interactions of
849 Exosomes and Other Extracellular Vesicles. Annu Rev Cell Dev Biol 30:255–289.

850 Dan B (2022) Developmental central hypotonia: implications for counselling, prognosis, and
851 management. Dev Med Child Neurol 64:4.

852 Davies BA, Azmi IF, Payne J, Shestakova A, Horazdovsky BF, Babst M, Katzmann DJ (2010)
853 Coordination of substrate binding and ATP hydrolysis in Vps4-mediated ESCRT-III
854 disassembly. Mol Biol Cell 21:3396–3408.

855 Dilsiz N (2020) Role of exosomes and exosomal microRNAs in cancer. Future Sci OA 6:FSO465.

856 Dobrowolski R, De Robertis EM (2012) Endocytic control of growth factor signalling:
857 multivesicular bodies as signalling organelles. Nat Rev Mol Cell Biol 13:53–60.

858 Duarte-Silva E, Oriá AC, Mendonça IP, de Melo MG, Paiva IHR, Maes M, Joca SRL, Peixoto CA
859 (2022) Tiny in size, big in impact: Extracellular vesicles as modulators of mood, anxiety
860 and neurodevelopmental disorders. Neurosci Biobehav Rev 135:104582.

861 Echteler SM (1984) Connections of the auditory midbrain in a teleost fish, Cyprinus carpio. J
862 Comp Neurol 230:536–551.

863 Edds-Walton PL, Fay RR (2008) Directional and frequency response characteristics in the
864 descending octaval nucleus of the toadfish (Opsanus tau). J Comp Physiol A 194:1013–
865 1029.

866 Erickson T, Morgan CP, Olt J, Hardy K, Busch-Nentwich E, Maeda R, Clemens R, Krey JF,
867 Nechiporuk A, Barr-Gillespie PG, Marcotti W, Nicolson T (2017) Integration of Tmc1/2
868 into the mechanotransduction complex in zebrafish hair cells is regulated by
869 Transmembrane O-methyltransferase (Tomt) Ginty DD, ed. eLife 6:e28474.

870 Frankel E, Shankar R, Moresco J, Yates J, Volkmann N, Audhya A (2017) Ist1 regulates ESCRT-III
871 assembly and function during multivesicular endosome biogenesis in Caenorhabditis
872 elegans embryos. Nat Commun 8.

873 Fukushima K (1987) The interstitial nucleus of Cajal and its role in the control of movements of
874 head and eyes. Prog Neurobiol 29:107–192.

875 Gahtan E, Sankrithi N, Campos JB, O'Malley DM (2002) Evidence for a widespread brain stem
876 escape network in larval zebrafish. J Neurophysiol 87:608–614.

877 Ganguly J, Kulshreshtha D, Almotiri M, Jog M (2021) Muscle Tone Physiology and Abnormalities.
878 Toxins 13:282.

879 Gao Y, Khan YA, Mo W, White KI, Perkins M, Pfuetzner RA, Trapani JG, Brunger AT, Nicolson T
880 (2023) Sensory deficit screen identifies nsf mutation that differentially affects SNARE
881 recycling and quality control. Cell Rep 42:112345.

882 Gao Y, Nicolson T (2021) Temporal Vestibular Deficits in synaptojanin 1 (synj1) Mutants. Front
883 Mol Neurosci 13:604189.

884 Gomes AR, Sangani NB, Fernandes TG, Diogo MM, Curfs LMG, Reutelingsperger CP (2020)
885 Extracellular Vesicles in CNS Developmental Disorders. Int J Mol Sci 21:9428.

886 González AE, Muñoz VC, Cavieres VA, Bustamante HA, Cornejo V-H, Januário YC, González I,
887 Hetz C, da Silva LL, Rojas-Fernández A, Hay RT, Mardones GA, Burgos PV (2017)
888 Autophagosomes cooperate in the degradation of intracellular C-terminal fragments of
889 the amyloid precursor protein via the MVB/lysosomal pathway. FASEB J 31:2446–2459.

890 Gurunathan S, Kang M-H, Kim J-H (2021) A Comprehensive Review on Factors Influences
891 Biogenesis, Functions, Therapeutic and Clinical Implications of Exosomes. Int J
892 Nanomedicine 16:1281–1312.

893 Gurung S, Perocheau D, Touramanidou L, Baruteau J (2021) The exosome journey: from
894 biogenesis to uptake and intracellular signalling. Cell Commun Signal CCS 19:47.

895 Haffter P, Granato M, Brand M, Mullins MC, Hammerschmidt M, Kane DA, Odenthal J, van
896 Eeden FJ, Jiang YJ, Heisenberg CP, Kelsh RN, Furutani-Seiki M, Vogelsang E, Beuchle D,
897 Schach U, Fabian C, Nusslein-Volhard C (1996) The identification of genes with unique
898 and essential functions in the development of the zebrafish, Danio rerio. Development
899 123:1–36.

900 Hamling KR, Harmon K, Kimura Y, Higashijima S, Schoppik D (2023a) The vestibulospinal nucleus
901 is a locus of balance development. bioRxiv:2023.12.06.570482.

902 Hamling KR, Harmon K, Schoppik D (2023b) The Nature and Origin of Synaptic Inputs to
903 Vestibulospinal Neurons in the Larval Zebrafish. eNeuro 10:ENEURO.0090-23.2023.

904 Han W, Zhang H, Feng L, Dang R, Wang J, Cui C, Jiang P (2023) The emerging role of exosomes in
905 communication between the periphery and the central nervous system. MedComm
906 4:e410.

907 Hanovice NJ, Daly CMS, Gross JM (2015) N-Ethylmaleimide–Sensitive Factor b (nsfb) Is Required
908 for Normal Pigmentation of the Zebrafish Retinal Pigment Epithelium. Invest
909 Ophthalmol Vis Sci 56:7535–7544.

910 Hou L, Liu K, Li Y, Ma S, Ji X, Liu L (2016) Necrotic pyknosis is a morphologically and
911 biochemically distinct event from apoptotic pyknosis. J Cell Sci 129:3084–3090.

912 Inoue M, Tanimoto M, Oda Y (2013) The role of ear stone size in hair cell acoustic sensory
913 transduction. Sci Rep 3:2114.

914 Jia Y, Bagnall MW (2022) Monosynaptic targets of utricular afferents in the larval zebrafish.
915 Front Neurol 13 Available at: https://www.ncbi.nlm.nih.gov/pmc/articles/PMC9355653/
916 [Accessed February 22, 2024].

917 Kalluri R, LeBleu VS (2020) The biology, function, and biomedical applications of exosomes.
918 Science 367:eaau6977.

919 Kim D, Pertea G, Trapnell C, Pimentel H, Kelley R, Salzberg SL (2013) TopHat2: accurate
920 alignment of transcriptomes in the presence of insertions, deletions and gene fusions.
921 Genome Biol 14:R36.

922 Kist AM, Portugues R (2019) Optomotor Swimming in Larval Zebrafish Is Driven by Global
923 Whole-Field Visual Motion and Local Light-Dark Transitions. Cell Rep 29:659-670.e3.

924 Knapik EW, Goodman A, Ekker M, Chevrette M, Delgado J, Neuhauss S, Shimoda N, Driever W,
925 Fishman MC, Jacob HJ (1998) A microsatellite genetic linkage map for zebrafish (Danio
926 rerio). Nat Genet 18:338–343.

927 Kohashi T, Oda Y (2008) Initiation of Mauthner- or Non-Mauthner-Mediated Fast Escape Evoked
928 by Different Modes of Sensory Input. J Neurosci 28:10641–10653.

929 Koyama M, Kinkhabwala A, Satou C, Higashijima S, Fetcho J (2011) Mapping a sensory-motor
930 network onto a structural and functional ground plan in the hindbrain. Proc Natl Acad
931 Sci 108:1170–1175.

932 Kroll F, Powell GT, Ghosh M, Gestri G, Antinucci P, Hearn TJ, Tunbak H, Lim S, Dennis HW,
933 Fernandez JM, Whitmore D, Dreosti E, Wilson SW, Hoffman EJ, Rihel J (2021) A simple
934 and effective F0 knockout method for rapid screening of behaviour and other complex
935 phenotypes Ekker SC, Stainier DY, Balciunas D, eds. eLife 10:e59683.

936 Labun K, Montague TG, Krause M, Torres Cleuren YN, Tjeldnes H, Valen E (2019) CHOPCHOP v3:
937 expanding the CRISPR web toolbox beyond genome editing. Nucleic Acids Res 47:W171–
938 W174.

939 Lacoste AMB, Schoppik D, Robson DN, Haesemeyer M, Portugues R, Li JM, Randlett O, Wee CL,
940 Engert F, Schier AF (2015) A convergent and essential interneuron pathway for
941 Mauthner-cell-mediated escapes. Curr Biol CB 25:1526–1534.

942 Leshchiner I, Alexa K, Kelsey P, Adzhubei I, Austin-Tse CA, Cooney JD, Anderson H, King MJ,
943 Stottmann RW, Garnaas MK, Ha S, Drummond IA, Paw BH, North TE, Beier DR, Goessling
944 W, Sunyaev SR (2012) Mutation mapping and identification by whole-genome
945 sequencing. Genome Res 22:1541–1548.

946 Leung LC, Wang GX, Madelaine R, Skariah G, Kawakami K, Deisseroth K, Urban AE, Mourrain P
947 (2019) Neural signatures of sleep in zebrafish. Nature 571:198–204.

948 Lewis EM, Kroll KL (2018) Development and disease in a dish: the epigenetics of
949 neurodevelopmental disorders. Epigenomics 10:219–231.

950 Lim Y-J, Lee S-J (2017) Are exosomes the vehicle for protein aggregate propagation in
951 neurodegenerative diseases? Acta Neuropathol Commun 5:64.

952 Liu Z, Bagnall MW (2023) Organization of vestibular circuits for postural control in zebrafish.
953 Curr Opin Neurobiol 82:102776.

954 Liu Z, Hildebrand DGC, Morgan JL, Jia Y, Slimmon N, Bagnall MW (2022) Organization of the
955 gravity-sensing system in zebrafish. Nat Commun 13:5060.

956 Loncle N, Agromayor M, Martin-Serrano J, Williams DW (2015) An ESCRT module is required for
957 neuron pruning. Sci Rep 5:8461.

958 López-Schier H (2019) Neuroplasticity in the acoustic startle reflex in larval zebrafish. Curr Opin
959 Neurobiol 54:134–139.

960 Lunati A, Petit A, Lapillonne H, Gameiro C, Saillour V, Garel C, Doummar D, Qebibo L, Aissat A,
961 Fanen P, Bartolucci P, Galactéros F, Funalot B, Burglen L, Mansour-Hendili L (2021)
962 VPS4A mutation in syndromic congenital hemolytic anemia without obvious signs of
963 dyserythropoiesis. Am J Hematol 96:E121–E123.

964 Makhankov YV, Rinner O, Neuhauss SCF (2004) An inexpensive device for non-invasive
965 electroretinography in small aquatic vertebrates. J Neurosci Methods 135:205–210.

966 Marsden KC, Granato M (2015) In vivo Ca2+ imaging reveals that decreased dendritic
967 excitability drives startle habituation. Cell Rep 13:1733–1740.

968 Matsuda K, Kubo F (2021) Circuit Organization Underlying Optic Flow Processing in Zebrafish.
969 Front Neural Circuits 15 Available at:
970 https://www.frontiersin.org/articles/10.3389/fncir.2021.709048 [Accessed February 28,
971 2024].

972 McCormick CA (1999) Anatomy of the Central Auditory Pathways of Fish and Amphibians. In:
973 Comparative Hearing: Fish and Amphibians (Fay RR, Popper AN, eds), pp 155–217
974 Springer Handbook of Auditory Research. New York, NY: Springer. Available at:
975 https://doi.org/10.1007/978-1-4612-0533-3_5 [Accessed February 22, 2024].

976 McCullough J, Frost A, Sundquist WI (2018) Structures, Functions, and Dynamics of ESCRT-
977 III/Vps4 Membrane Remodeling and Fission Complexes. Annu Rev Cell Dev Biol 34:85–
978 109.

979 Meldolesi J (2018) Exosomes and Ectosomes in Intercellular Communication. Curr Biol 28:R435–
980 R444.

981 Migault G, van der Plas TL, Trentesaux H, Panier T, Candelier R, Proville R, Englitz B, Debrégeas
982 G, Bormuth V (2018) Whole-Brain Calcium Imaging during Physiological Vestibular
983 Stimulation in Larval Zebrafish. Curr Biol 28:3723-3735.e6.

984 Mirat O, Sternberg JR, Severi KE, Wyart C (2013) ZebraZoom: an automated program for high-
985 throughput behavioral analysis and categorization. Front Neural Circuits 7:107.

986 Mo W, Chen F, Nechiporuk A, Nicolson T (2010) Quantification of vestibular-induced eye
987 movements in zebrafish larvae. BMC Neurosci 11:110.

988 Monroe N, Han H, Gonciarz MD, Eckert DM, Karren MA, Whitby FG, Sundquist WI, Hill CP (2014)
989 The oligomeric state of the active Vps4 AAA ATPase. J Mol Biol 426:510–525.

990 Muto A, Ohkura M, Abe G, Nakai J, Kawakami K (2013) Real-Time Visualization of Neuronal
991 Activity during Perception. Curr Biol 23:307–311.

992 Nicolson T (2017) The genetics of hair-cell function in zebrafish. J Neurogenet 31:102–112.

993 Niklaus S, Cadetti L, Berg-Maurer CM vom, Lehnherr A, Hotz AL, Forster IC, Gesemann M,
994 Neuhauss SCF (2017) Shaping of Signal Transmission at the Photoreceptor Synapse by
995 EAAT2 Glutamate Transporters. eNeuro 4 Available at:
996 https://www.eneuro.org/content/4/3/eneuro.0339-16.2017 [Accessed May 16, 2023].

997 Ott C, Nachmias D, Adar S, Jarnik M, Sherman S, Birnbaum RY, Lippincott-Schwartz J, Elia N
998 (2018) VPS4 is a dynamic component of the centrosome that regulates centrosome
999 localization of γ-tubulin, centriolar satellite stability and ciliogenesis. Sci Rep 8:3353.

1000 Palmulli R, van Niel G (2018) To be or not to be... secreted as exosomes, a balance finely tuned
1001 by the mechanisms of biogenesis Stahl P, Raposo G, eds. Essays Biochem 62:177–191.

1002 Parenti I, Rabaneda LG, Schoen H, Novarino G (2020) Neurodevelopmental Disorders: From
1003 Genetics to Functional Pathways. Trends Neurosci 43:608–621.

1004 Piper RC, Katzmann DJ (2007) Biogenesis and Function of Multivesicular Bodies. Annu Rev Cell
1005 Dev Biol 23:519–547.

1006 Privat M, Romano SA, Pietri T, Jouary A, Boulanger-Weill J, Elbaz N, Duchemin A, Soares D,
1007 Sumbre G (2019) Sensorimotor Transformations in the Zebrafish Auditory System. Curr
1008 Biol 29:4010-4023.e4.

1009 Rodger C et al. (2020) De Novo VPS4A Mutations Cause Multisystem Disease with Abnormal
1010 Neurodevelopment. Am J Hum Genet 107:1129–1148.

1011 Sankrithi NS, O'Malley DM (2010) Activation of a multisensory, multifunctional nucleus in the
1012 zebrafish midbrain during diverse locomotor behaviors. Neuroscience 166:970–993.

1013 Scheuring S, Röhricht RA, Schöning-Burkhardt B, Beyer A, Müller S, Abts HF, Köhrer K (2001)
1014 Mammalian cells express two VPS4 proteins both of which are involved in intracellular
1015 protein trafficking. J Mol Biol 312:469–480.

1016 Sehnal D, Bittrich S, Deshpande M, Svobodová R, Berka K, Bazgier V, Velankar S, Burley SK, Koča
1017 J, Rose AS (2021) Mol* Viewer: modern web app for 3D visualization and analysis of
1018 large biomolecular structures. Nucleic Acids Res 49:W431–W437.

1019 Seu KG, Trump LR, Emberesh S, Lorsbach RB, Johnson C, Meznarich J, Underhill HR, Chou ST,
1020 Sakthivel H, Nassar NN, Seu KJ, Blanc L, Zhang W, Lutzko CM, Kalfa TA (2020) VPS4A
1021 Mutations in Humans Cause Syndromic Congenital Dyserythropoietic Anemia due to
1022 Cytokinesis and Trafficking Defects. Am J Hum Genet 107:1149–1156.

1023 Severi KE, Portugues R, Marques JC, O'Malley DM, Orger MB, Engert F (2014) Neural Control
1024 and Modulation of Swimming Speed in the Larval Zebrafish. Neuron 83:692–707.

1025 Shimazaki T, Tanimoto M, Oda Y, Higashijima S (2019) Behavioral Role of the Reciprocal
1026 Inhibition between a Pair of Mauthner Cells during Fast Escapes in Zebrafish. J Neurosci
1027 39:1182–1194.

1028 Sillar KT (2009) Escape Behaviour: Reciprocal Inhibition Ensures Effective Escape Trajectory.
1029 Curr Biol 19:R697–R699.

1030 Smith ET, Pacentine I, Shipman A, Hill M, Nicolson T (2020) Disruption of tmc1/2a/2b Genes in
1031 Zebrafish Reveals Subunit Requirements in Subtypes of Inner Ear Hair Cells. J Neurosci
1032 40:4457–4468.

1033 Strausberg RL et al. (2002) Generation and initial analysis of more than 15,000 full-length
1034 human and mouse cDNA sequences. Proc Natl Acad Sci U S A 99:16899–16903.

1035 Sugioka T, Tanimoto M, Higashijima S (2023) Biomechanics and neural circuits for vestibular-
1036 induced fine postural control in larval zebrafish. Nat Commun 14:1217.

1037 Sun P, Zhang Y, Zhao F, Wu J-P, Pun SH, Peng C, Du M, Vai MI, Liu D, Chen F (2018) An Assay for
1038 Systematically Quantifying the Vestibulo-Ocular Reflex to Assess Vestibular Function in
1039 Zebrafish Larvae. Front Cell Neurosci 12:257.

1040 Sun S, Li L, Yang F, Wang X, Fan F, Yang M, Chen C, Li X, Wang H-W, Sui S-F (2017) Cryo-EM
1041 structures of the ATP-bound Vps4E233Q hexamer and its complex with Vta1 at near-
1042 atomic resolution. Nat Commun 8:16064.

1043 Tanimoto M, Ota Y, Horikawa K, Oda Y (2009) Auditory input to CNS is acquired coincidentally
1044 with development of inner ear after formation of functional afferent pathway in
1045 zebrafish. J Neurosci Off J Soc Neurosci 29:2762–2767.

1046 Tanimoto M, Watakabe I, Higashijima S (2022) Tiltable objective microscope visualizes
1047 selectivity for head motion direction and dynamics in zebrafish vestibular system. Nat
1048 Commun 13:7622.

1049 Thiele TR, Donovan JC, Baier H (2014) Descending Control of Swim Posture by a Midbrain
1050 Nucleus in Zebrafish. Neuron 83:679–691.

1051 Vanwalleghem G, Heap LA, Scott EK (2017) A profile of auditory-responsive neurons in the
1052 larval zebrafish brain. J Comp Neurol 525:3031–3043.

1053 Verweij FJ et al. (2018) Quantifying exosome secretion from single cells reveals a modulatory
1054 role for GPCR signaling. J Cell Biol 217:1129–1142.

1055 Verweij FJ, Revenu C, Arras G, Dingli F, Loew D, Pegtel DM, Follain G, Allio G, Goetz JG,
1056 Zimmermann P, Herbomel P, Del Bene F, Raposo G, van Niel G (2019) Live Tracking of
1057 Inter-organ Communication by Endogenous Exosomes In Vivo. Dev Cell 48:573-589.e4.

1058 Wang W-C, McLean DL (2014) Selective Responses to Tonic Descending Commands by
1059 Temporal Summation in a Spinal Motor Pool. Neuron 83:708–721.

1060 Waqas MY, Javid MA, Nazir MM, Niaz N, Nisar MF, Manzoor Z, Bhatti SA, Hameed S, Khaliq MH
1061 (2022) Extracellular vesicles and exosome: insight from physiological regulatory
1062 perspectives. J Physiol Biochem 78:573–580.

1063 Wehner D, Becker T, Becker CG (2017) Restoration of anatomical continuity after spinal cord
1064 transection depends on Wnt/β-catenin signaling in larval zebrafish. Data Brief 16:65–70.

1065 Westerfield M (2000) The Zebrafish Book. A Guide for the Laboratory Use of Zebrafish (Danio
1066 rerio), 4th Edition. University of Oregon Press.

1067 Willén K, Edgar JR, Hasegawa T, Tanaka N, Futter CE, Gouras GK (2017) Aβ accumulation causes
1068 MVB enlargement and is modelled by dominant negative VPS4A. Mol Neurodegener
1069 12:61.

1070 Woods IG, Lyons DA, Voas MG, Pogoda H-M, Talbot WS (2006) nsf Is Essential for Organization
1071 of Myelinated Axons in Zebrafish. Curr Biol 16:636–648.

1072 Wu RS, Lam II, Clay H, Duong DN, Deo RC, Coughlin SR (2018) A Rapid Method for Directed
1073 Gene Knockout for Screening in G0 Zebrafish. Dev Cell 46:112-125.e4.

1074 Xu L, Guan NN, Huang C-X, Hua Y, Song J (2021) A neuronal circuit that generates the temporal
1075 motor sequence for the defensive response in zebrafish larvae. Curr Biol 31:3343-
1076 3357.e4.

1077 Yang Q et al. (2016) A splicing mutation in VPS4B causes dentin dysplasia I. J Med Genet
1078 53:624–633.

1079 Yari H, Mikhailova MV, Mardasi M, Jafarzadehgharehziaaddin M, Shahrokh S, Thangavelu L,
1080 Ahmadi H, Shomali N, Yaghoubi Y, Zamani M, Akbari M, Alesaeidi S (2022) Emerging role
1081 of mesenchymal stromal cells (MSCs)-derived exosome in neurodegeneration-
1082 associated conditions: a groundbreaking cell-free approach. Stem Cell Res Ther 13:423.

1083 Zhang X, Jiang W, Lu Y, Mao T, Gu Y, Ju D, Dong C (2023) Exosomes combined with biomaterials
1084 in the treatment of spinal cord injury. Front Bioeng Biotechnol 11:1077825.

1085 Zhang Y, Liu Y, Liu H, Tang WH (2019) Exosomes: biogenesis, biologic function and clinical
1086 potential. Cell Biosci 9:19.

1087

1088 **FIGURES**

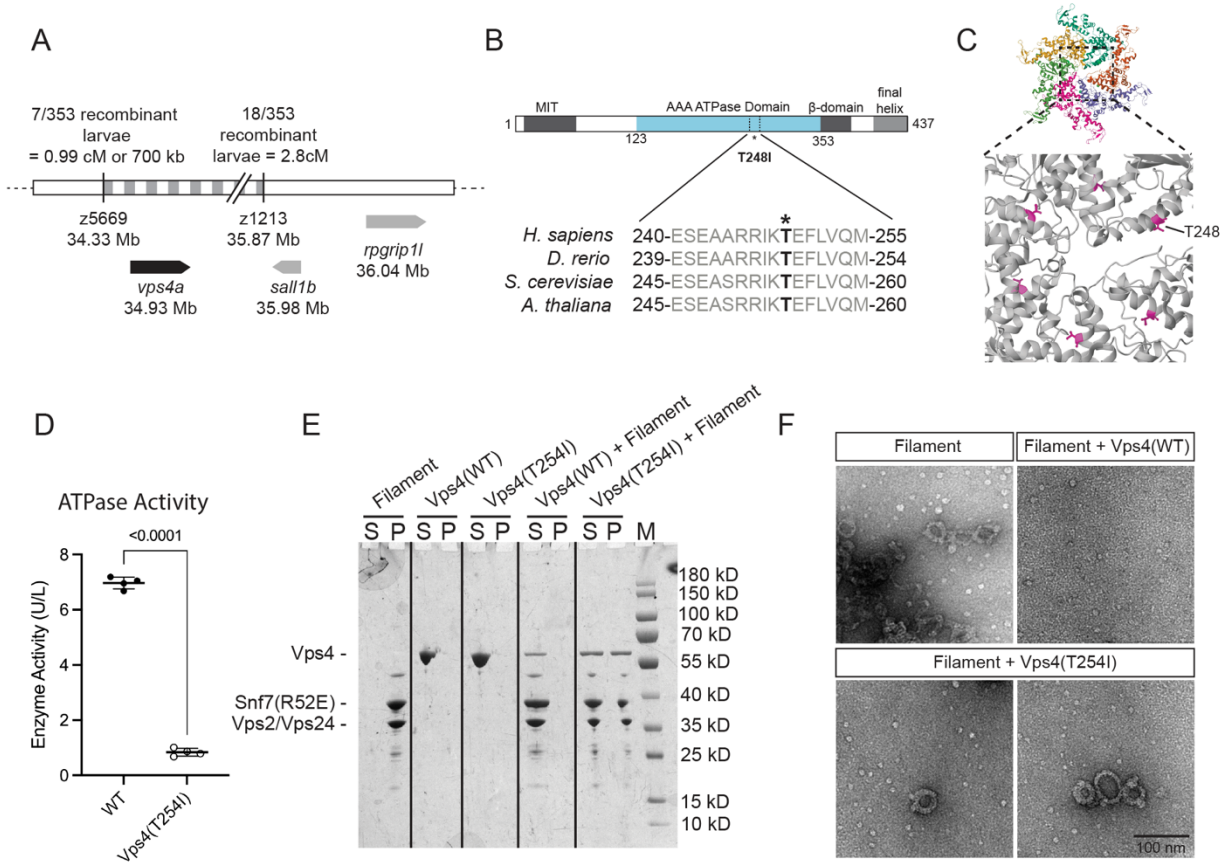

1089

1090 **Figure 1. The T248I mutation in *vps4a* reduces ATPase activity and ESCRT-III filament**
1091 **disassembly. A,** *vps4a* is located on Chromosome 25 in a location corresponding to where
1092 classical mapping methods have identified the location of the gene responsible for the
1093 *raumschiff* phenotypes. **B,** Bar diagram of Vps4a protein showing the location of the T248I
1094 mutation. **C,** Atomic model structure of the $Vps4^{E233Q}$ hexamer, with T248 marked in magenta
1095 (Image adapted from the RCSB PDB ID:5XMI, using Mol*). **D,** Mutant Vps4 (T254I) yeast
1096 protein has decreased ATP activity compared to wild-type Vps4 protein. Unpaired t test, $p <$
1097 0.0001, $n_{WT} = 4$, $n_{vps4(T254I)} = 4$, $t = 47.92$, df = 6. **E,** Sedimentation analysis of Vps4 and
1098 Vps4(T254I)-mediated disassembly of ESCRT-III filaments. Pellet (P) and supernatant (S)
1099 fractions were analyzed by SDS-PAGE. Marker (M). **F,** Negative staining EM micrograph of
1100 sedimentation analysis of ESCRT-III filament disassembly.

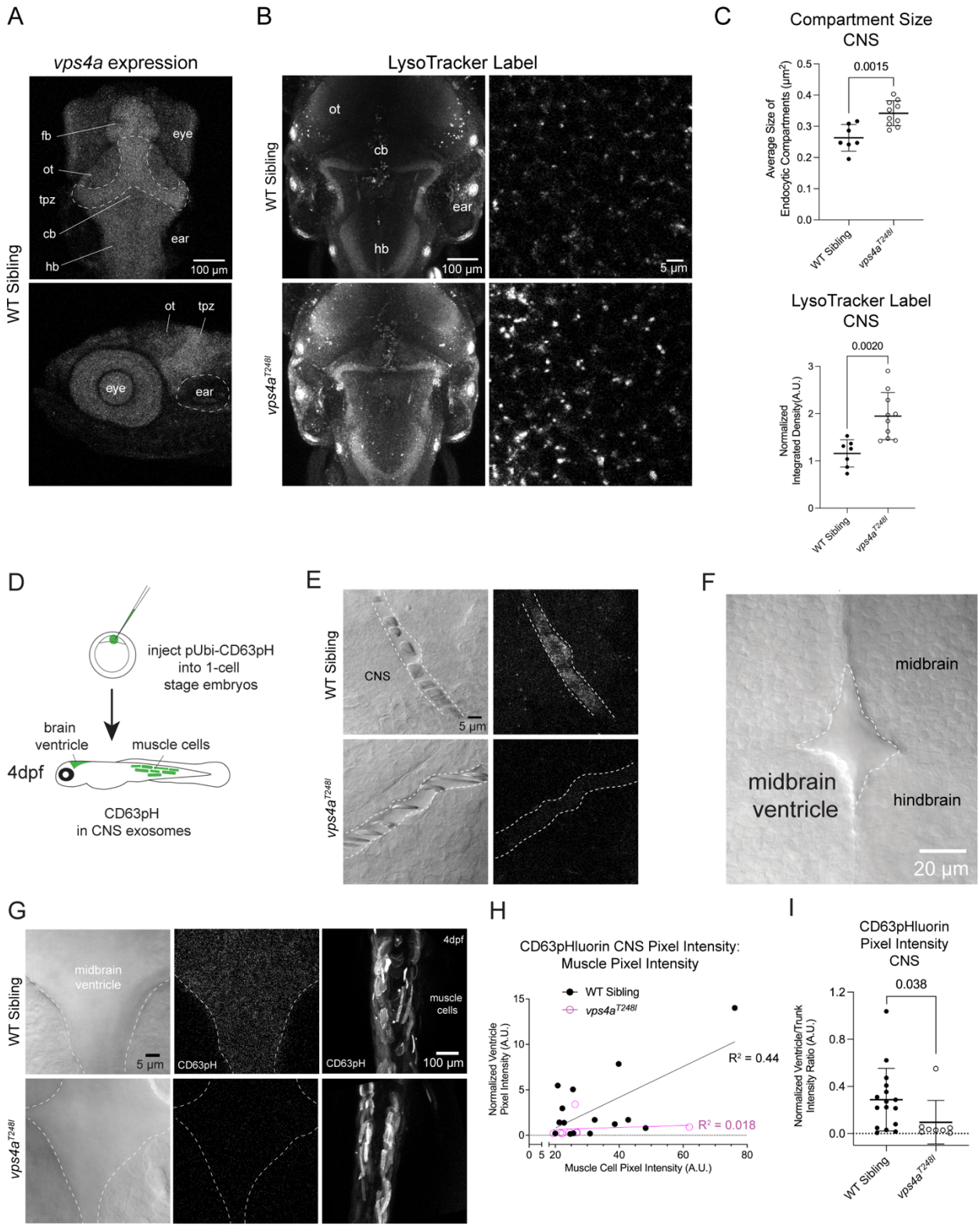
A
vps4a expression
WT Sibling
fb
eye
ot
tpz
cb
ear
hb
100 µm
ot
tpz
eye
ear
B
LysoTracker Label
WT Sibling
vps4aT248I
ot
cb
ear
hb
100 µm
5 µm
C
Compartment Size CNS
0.0015
Average Size of Endocytic Compartments (µm2)
WT Sibling
vps4aT248I
LysoTracker Label CNS
0.0020
Normalized Integrated Density(A.U.)
WT Sibling
vps4aT248I
D
inject pUbi-CD63pH into 1-cell stage embryos
brain ventricle
muscle cells
4dpf
CD63pH in CNS exosomes
E
WT Sibling
vps4aT248I
CNS
5 µm
F
midbrain
midbrain ventricle
hindbrain
20 µm
G
WT Sibling
vps4aT248I
midbrain ventricle
5 µm
CD63pH
4dpf
muscle cells
CD63pH
100 µm
H
CD63pHluorin CNS Pixel Intensity: Muscle Pixel Intensity
WT Sibling
vps4aT248I
R2 = 0.44
R2 = 0.018
Normalized Ventricle Pixel Intensity (A.U.)
Muscle Cell Pixel Intensity (A.U.)
I
CD63pHluorin Pixel Intensity CNS
0.038
Normalized Ventricle/Trunk Intensity Ratio (A.U.)
WT Sibling
vps4aT248I

1101

1102

1103 **Figure 2. *vps4a*^{T248I} mutants have enlarged endosomal compartments and release fewer**
1104 **exosomes in the CNS. A,** Confocal Z-projections of a 5 dpf wild-type zebrafish larva labeled
1105 with HCR RNA-FISH probes for *vps4a.* fb, forebrain; ot, optic tectum; tpz, tectal proliferation
1106 zone, cb, cerebellum; hb, hindbrain. **B,** LysoTracker staining of 5 dpf wild-type siblings and
1107 *vps4a*^{T248I} mutants show an increased staining in the mutant. **C,** Acidic membrane compartment
1108 size in the hindbrain of *vps4a*^{T248I} mutants (N = 10) is significantly larger than those in wild-type
1109 siblings (N = 7); unpaired t test, p = 0.0015, t = 3.873, df = 15. LysoTracker vital dye taken up
1110 by *vps4a*^{T248I} mutants (N = 10), measured as normalized pixel integrated density, is significantly
1111 higher compared to wild-type siblings (N =7); unpaired t test, p = 0.0020, t = 3.744, df = 15.
1112 **D,** Schematic of injecting 1-cell stage nacre-background embryos with pUbi:CD63-pHluorin.
1113 Healthy larvae were sorted on 1 dpf, and larvae expressing CD63-pHluorin in muscle cells was
1114 sorted on 3 dpf, for imaging on 4 dpf. **E,** Decreased CD63-pHluorin expression in 3 dpf
1115 *vps4a*^{T248I} mutant CNS blood vessels. **F,** Dorsal view of 4 dpf zebrafish larva showing the
1116 midbrain ventricle. **G,** Decreased CD63-pHluorin expression in *vps4a*^{T248I} mutant brain
1117 ventricles, but trunk muscles express comparable levels to wild-type siblings. **H,** Pixel intensity
1118 of muscles cells is correlated with normalized pixel intensity of CD63-pHluorin signal in the
1119 midbrain ventricle in wild-type siblings (N = 16). **I,** Quantification of CD63-pHluorin fluorescence
1120 in wild-type siblings (N = 16) and *vps4a*^{T248I} mutants (N = 8); Mann-Whitney test, p = 0.0382
1121 (exact).
1122

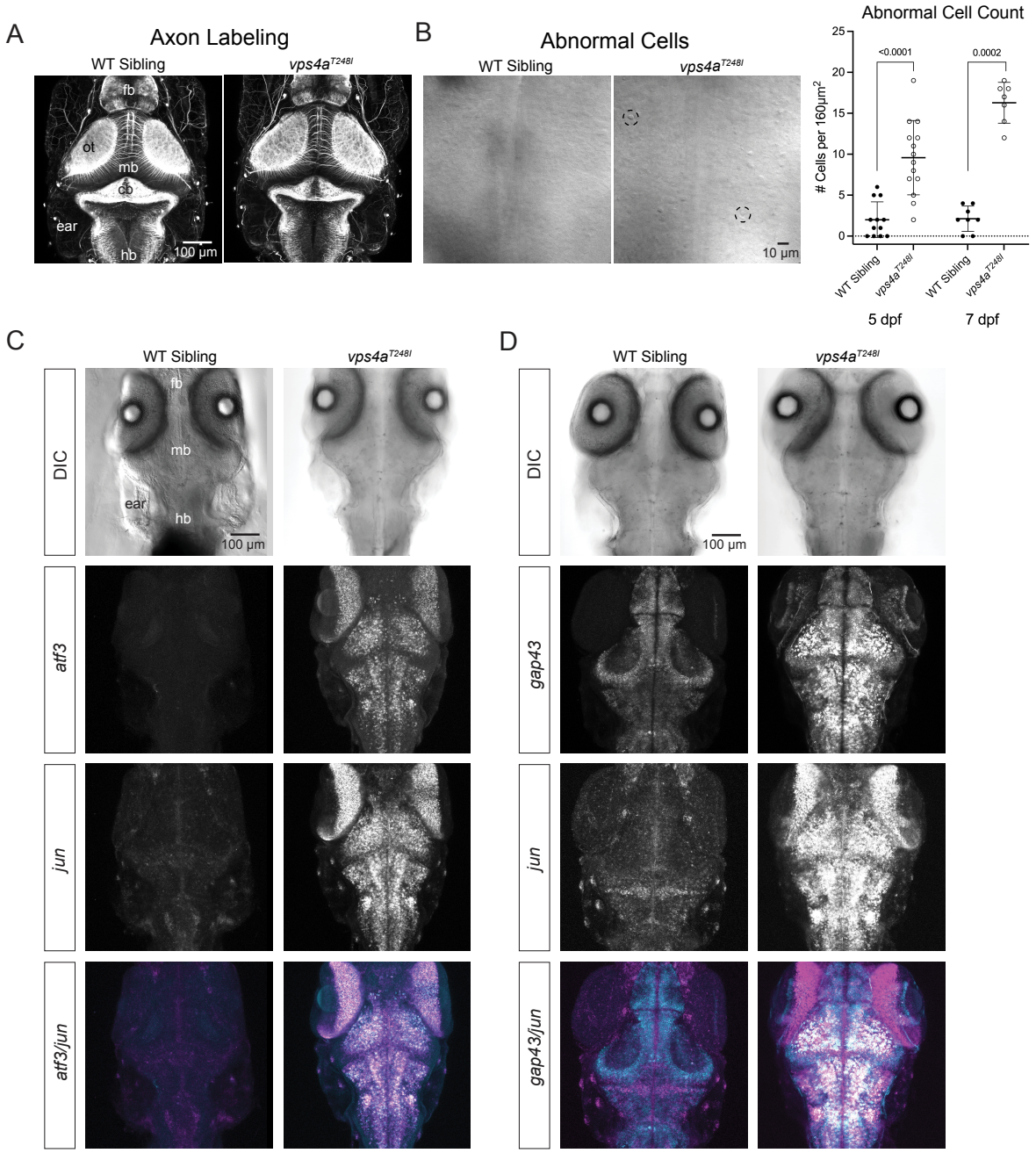

1123

1124 **Figure 3. *vps4a*^{T248I} mutants upregulate stress response and regeneration genes in the**

1125 **CNS. A,** Axons labeled with acetylated tubulin antibody staining of *vps4a*^{T248I} mutants show no

1126 gross morphological defects. Fb, forebrain; ot, optic tectum; mb, midbrain; cb, cerebellum; hb,

1127 hindbrain. **B,** *vps4a*^{T248I} mutants have an increase of morphologically abnormal, pyknotic cells

in the CNS. Two examples are highlighted with black dashed circles. The number of abnormal cells in the *vps4a*^{T248I} mutants was quantified and found to be significantly higher than in wild-type siblings at both 5 dpf and 7 dpf; Mann-Whitney test, 5 dpf, $p < 0.0001$ (exact), $n_{WT} = 12$, $n_{vps4a(T248I)} = 14$; 7 dpf, $p < 0.0002$ (exact), $n_{WT} = 8$, $n_{vps4a(T248I)} = 7$. **C,** Maximum intensity projections of *atf3* and *jun* mRNA expression in the hindbrain of 5 dpf wild-type sibling and *vps4a*^{T248I} mutants. **D,** Maximum intensity projections of *gap43* and *jun* mRNA expression in the hindbrain of 5 dpf wild-type sibling and *vps4a*^{T248I} mutants.

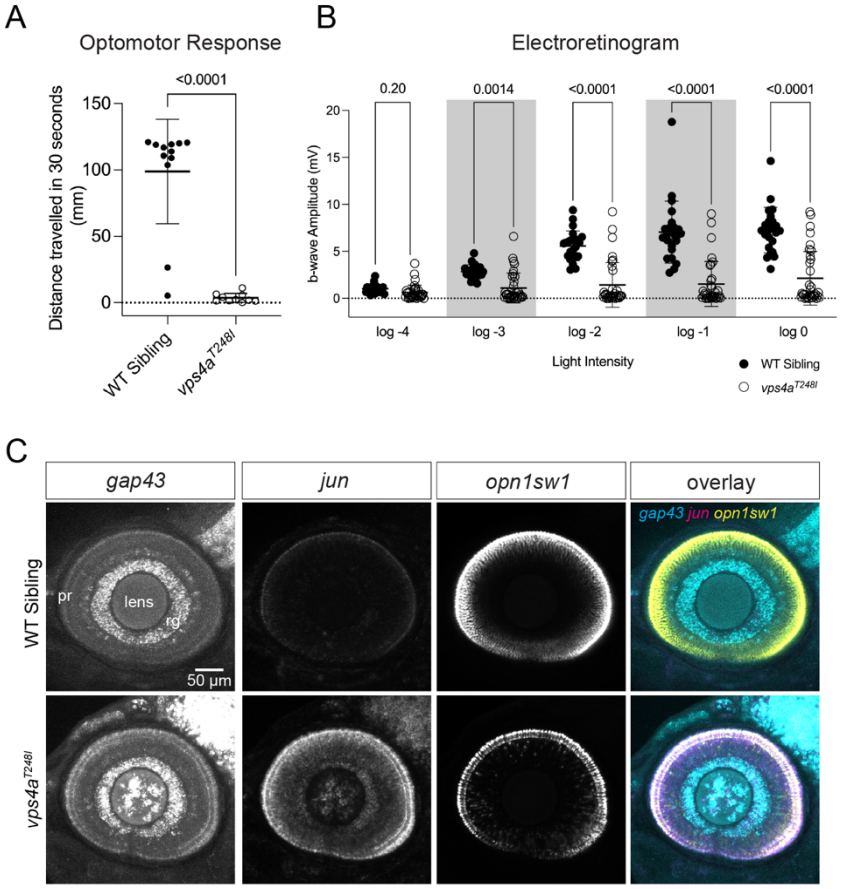

Figure 4. Impaired vision in *vps4a*^{T248I} mutants. A, 5 dpf *vps4a*^{T248I} mutants (N = 10) have a reduced optomotor response compared to wild-type siblings (N = 12); Mann-Whitney test, $p < 0.0001$ (exact). **B,** Decreased b wave amplitude in electroretinograms of 5-6 dpf *vps4a*^{T248I}

1140 mutants (N = 34) in comparison to wild-type siblings (N = 23) at brighter light intensities (log -4
1141 to log 0); Kruskal-Wallis test (log 0, $p < 0.0001$; log -1, $p < 0.0001$; log -2, $p < 0.0001$; log -3, $p =$
1142 0.0014; log -4, $p = 0.1989$). **C,** HCR RNA-FISH of *gap43*, *jun* and *opn1sw1* in the eye of
1143 *vps4a*^{T248I} mutants compared to wild-type siblings. Pr, photoreceptors; Rg, retinal ganglion cells,
1144 lens.
1145

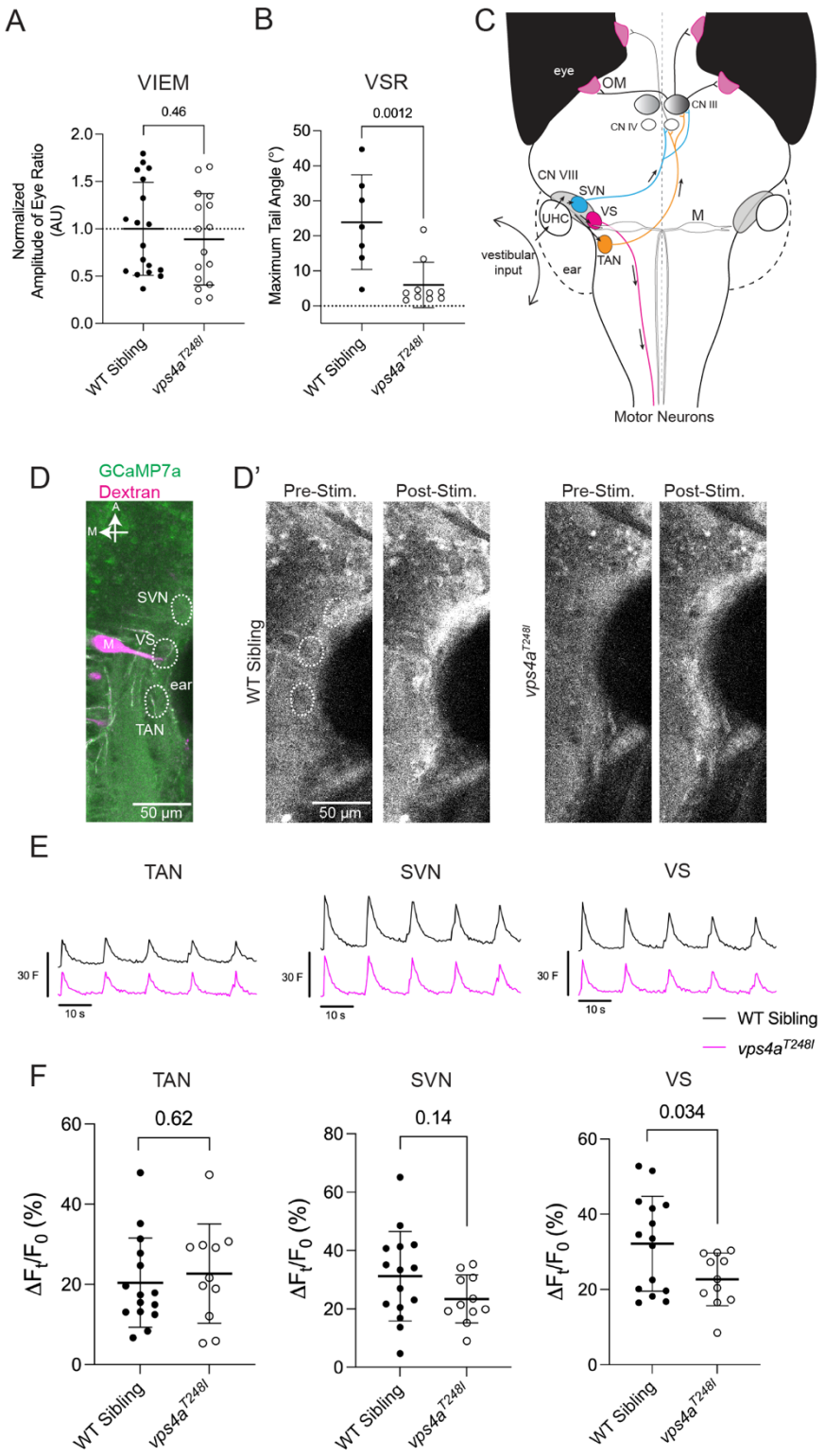
A
VIEM
0.46
Normalized Amplitude of Eye Ratio (AU)
2.0
1.5
1.0
0.5
0.0
WT Sibling
vps4a T248I
B
VSR
0.0012
Maximum Tail Angle (°)
50
40
30
20
10
0
WT Sibling
vps4a T248I
C
eye
OM
CN III
CN IV
CN VIII
SVN
UHC
VS
M
vestibular input
ear
TAN
Motor Neurons
D
GCaMP7a
Dextran
A
M
SVN
VS
M
ear
TAN
50 µm
D'
Pre-Stim.
Post-Stim.
WT Sibling
50 µm
Pre-Stim.
Post-Stim.
vps4a T248I
E
TAN
SVN
VS
30 F
10 s
WT Sibling
vps4a T248I
F
TAN
0.62
SVN
0.14
VS
0.034
ΔFt/F0 (%)
WT Sibling
vps4a T248I

1146

1147 **Figure 5. *vps4a*^{T248I} mutants have selective defects in vestibular circuitry. A,** 5 dpf
1148 *vps4a*^{T248I} mutants (N = 16) do not have a significantly different VIEM compared to wild-type
1149 siblings (N = 18); Mann-Whitney text, p = 0.4632 (exact). **B,** 5 dpf *vps4a*^{T248I} mutants (N = 10)
1150 have a reduced VSR compared to wild-type siblings (N = 7); Mann Whitney test, p = 0.0012
1151 (exact). **C,** Simplified schematic showing the flow of information evoked by head rotation from
1152 the inner ear to hindbrain nuclei, vestibulo-ocular neurons, and motor neurons. UHC, utricular
1153 hair cells; CN VIII, VIIIth nerve; SVN, superior vestibular nucleus; VS, vestibulospinal cells;
1154 TAN, tangential neurons; M, Mauthner cell; CN IV, trochlear nucleus; CN III, oculomotor
1155 nucleus; OM, oculomotor muscles. **D,** 5 dpf larva showing basal GCamP7a expression and
1156 backfill injected Rhodamine-Dextran marking the Mauthner cell. White dotted lines mark the
1157 TAN, SVN and VS. **D'** Pre- and post-stimulus GCaMP7a levels in vestibular region in a
1158 representative wild-type sibling and *vps4a*^{T248I} mutant. The TAN, SVN and VS ROIs are
1159 outlined by dotted lines. **E,** Average trace of normalized fluorescence (F) for the TAN, SVN and
1160 VS of wild-type siblings and *vps4a*^{T248I} mutants during auditory stimulation at 600Hz. **F,**
1161 Percentage change in fluorescence of the TAN, SVN and VS of wild-type siblings and *vps4a*^{T248I}
1162 mutants during auditory stimulation at 600Hz. The VS in *vps4a*^{T248I} mutants (N = 11) have a
1163 reduced change in fluorescence compared to wild-type siblings (N = 15); unpaired t test, p =
1164 0.0337 (exact), t = 2.252, df = 24. There is no significant difference between mutants and wild-
1165 type siblings in the TAN (unpaired t test, p = 0.1405 (exact), t = 1.524, df = 24) or SVN
1166 (unpaired t test, p = 0.6224 (exact), t = 0.4988, df = 24).
1167

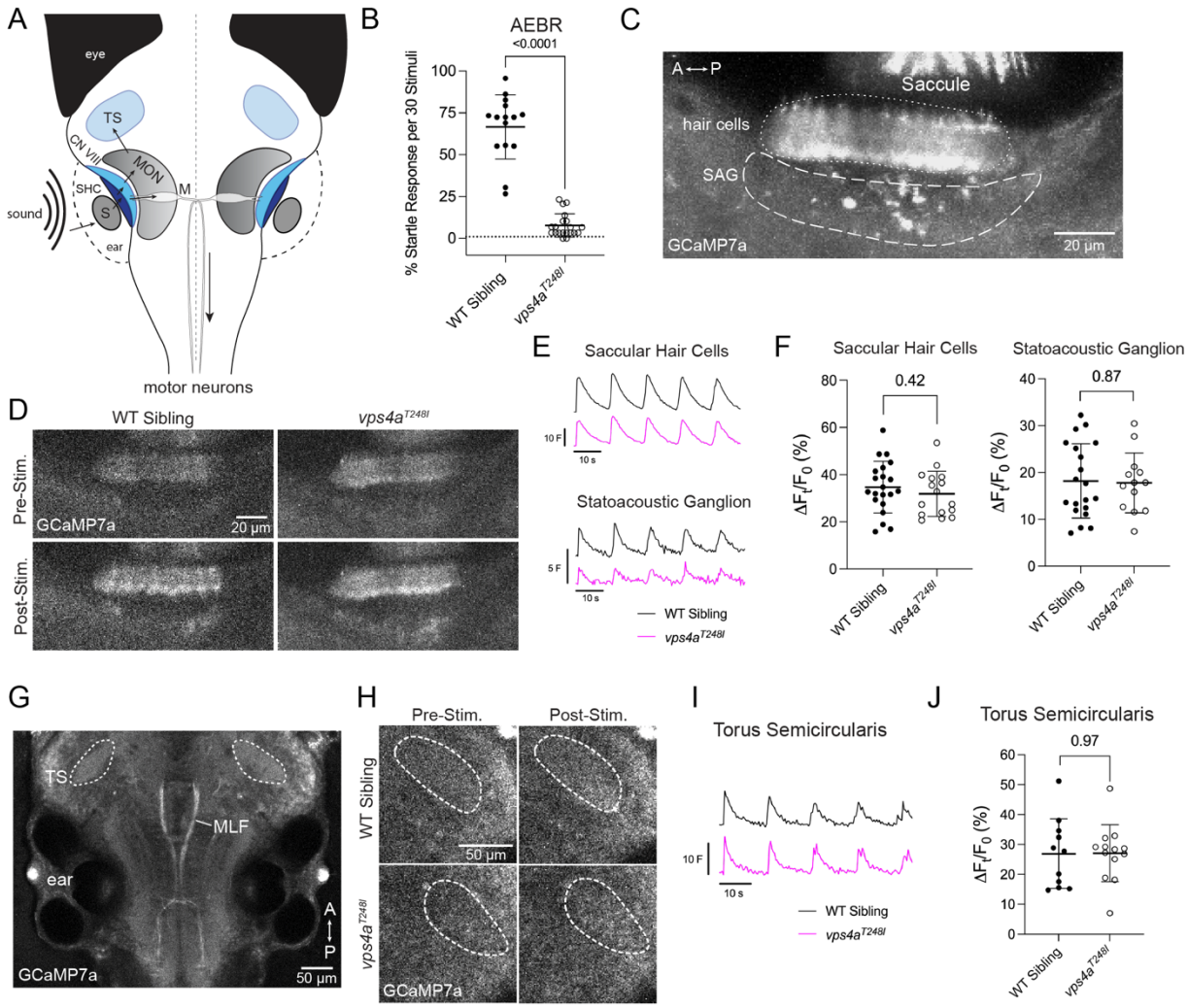

Figure 6. Activation of the ascending auditory pathway in *vps4a*^{T248I} mutants. A, Simplified schematic showing the flow of information from an auditory stimulus to motor neurons or to the torus semicircularis. S, saccular otolith; SHC, saccular hair cells; CN VIII, VIIIth nerve; MON, medial octavolateralis nucleus; M, Mauthner cell; TS, torus semicircularis. **B,** 5 dpf *vps4a*^{T248I} mutants (N = 20) have a greatly reduced AEBR compared to wild-type siblings (N = 15); Mann-Whitney test, $p < 0.0001$ (exact). **C,** Basal levels of GCaMP7a expression in the inner ear of 5 dpf larvae, focusing on the saccular hair cells (dotted line) and statoacoustic ganglion (SAG) (dashed line). **D,** Pre- and post-stimulus GCaMP7a levels in saccular hair cells and SAG in a representative wild-type sibling and *vps4a*^{T248I} mutant larvae. **E,** Average traces of normalized

1178 fluorescence (F) for the saccular hair cells and SAG of wild-type siblings and *vps4a*^{T248I} mutants
1179 during auditory stimulation at 600Hz. **F,** Percentage change in fluorescence of the saccular hair
1180 cells and SAG of wild-type siblings and *vps4a*^{T248I} mutants during auditory stimulation at 600Hz.
1181 There is no significant difference between mutants (N = 13) and wild-type siblings (N = 20) in
1182 the saccular hair cells (unpaired t test, p = 0.4162 (exact), t = 0.8228, df = 35) or the SAG
1183 (unpaired t test, p = 0.8748 (exact), t = 0.1588, df = 31). **G,** Representative image of 5 dpf
1184 zebrafish basal levels of GCaMP7a expression in the torus semicircularis (TS). **H,** Pre-and
1185 post-stimulus GCaMP7a levels in the TS in representative wild-type sibling and *vps4a*^{T248I}
1186 mutant larvae. **I,** Average trace of normalized fluorescence (F) for the TS of wild-type siblings
1187 and *vps4a*^{T248I} mutants during auditory stimulation at 600Hz. **J,** There is no significant
1188 difference in percentage change fluorescence between *vps4a*^{T248I} mutants (N = 13) and wild-
1189 type siblings (N = 11) in the TS; unpaired t test, p = 0.9672 (exact), t = 0.04157, df = 22.

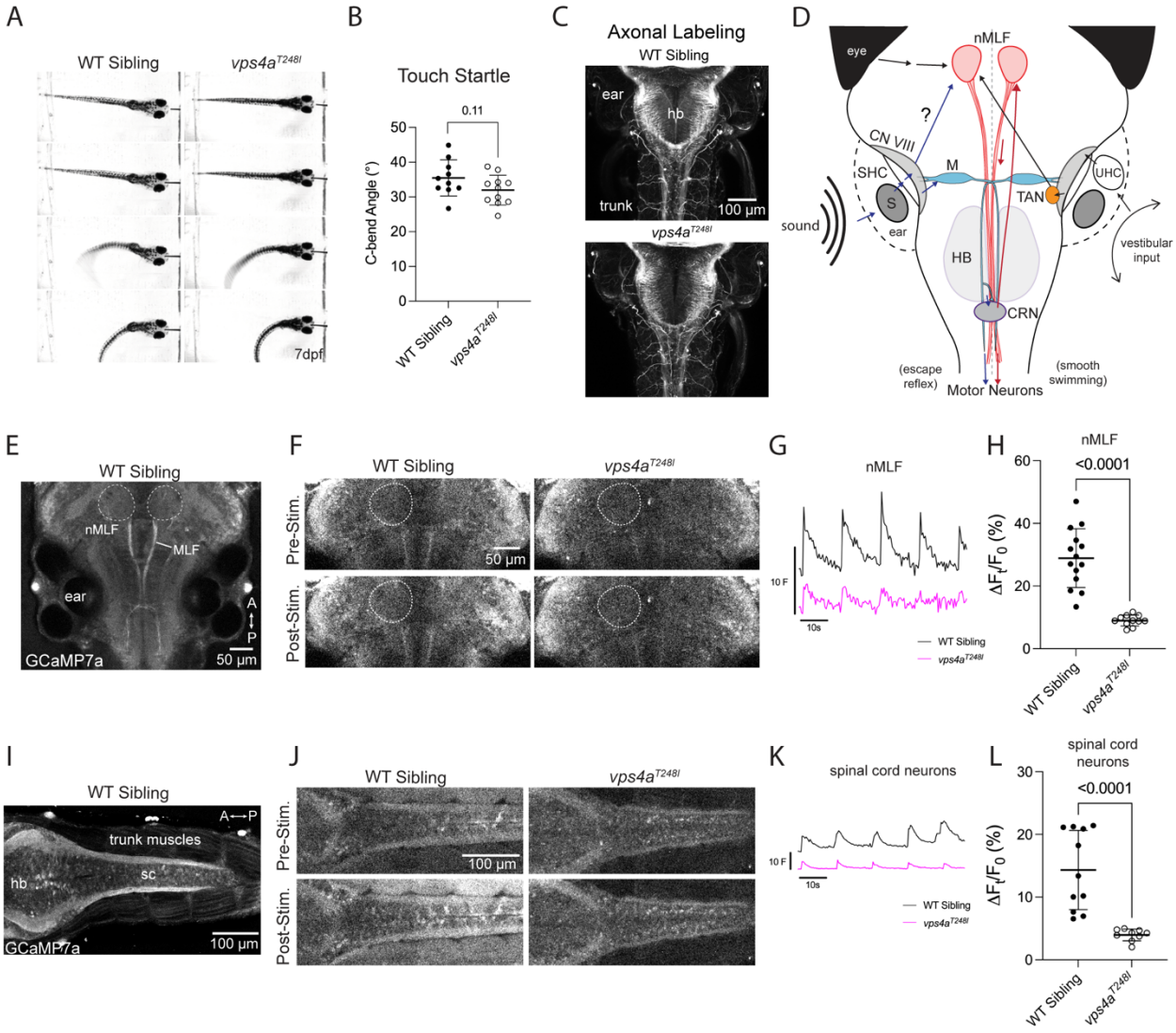

Figure 7. *vps4a^{T248I}* mutants display defects in sensorimotor transformation. **A,** 7 dpf *vps4a^{T248I}* mutant larvae have an intact startle reflex when touched. **B,** 7 dpf *vps4a^{T248I}* mutants (N = 11) do not have a significantly different C-bend angle compared to wild-type siblings (N = 10); unpaired t test, p = 0.1079 (exact), t = 1.687, df = 19. **C,** Acetylated tubulin antibody staining of *vps4a^{T248I}* mutants shows no gross morphological defects in hindbrain/spinal cord or somatosensory axons. **D,** Simplified schematic showing the flow of information from a tone stimulus from the inner ear to motor neurons via Mauthner cell and nMLF pathways. S, saccular otolith; SHC, saccular hair cells; CN VIII, VIIIth nerve; M, Mauthner cell; HB, hindbrain; CRN, cranial relay neurons; nMLF, nucleus of the medial longitudinal fasciculus. **E,**

1200 Representative image of 5 dpf zebrafish, showing location of nMLF expressing basal levels of
1201 GCaMP7a. **F,** Pre- and post-stimulus GCaMP7a levels in the nMLF in a representative wild-
1202 type sibling and *vps4a*^{T248I} mutant. **G,** Average trace of normalized fluorescence (F) for the
1203 nMLF of wild-type siblings and *vps4a*^{T248I} mutants during tone stimulation at 600Hz. **H,**
1204 *vps4a*^{T248I} mutants (N = 11) have a significantly reduced percentage change fluorescence in the
1205 nMLF compared to wild-type siblings (N = 14); unpaired t test, $p < 0.0001$ (exact), $t = 6.937$, df =
1206 23. **I,** Representative image of 5 dpf zebrafish trunk showing spinal cord neurons expressing
1207 basal levels of GCaMP7a. **J,** Pre-and post-stimulus GCaMP7a levels in the spinal cord motor
1208 neurons of representative wild-type sibling and *vps4a*^{T248I} mutant. **K,** Average trace of
1209 normalized fluorescence (F) for the spinal cord motor neurons of wild-type siblings and
1210 *vps4a*^{T248I} mutants during tone stimulation at 450Hz. **L,** *vps4a*^{T248I} mutants (N = 9) have a
1211 significantly reduced percentage change fluorescence in spinal cord neurons compared to wild-
1212 type siblings (N = 11), Mann-Whitney test, $p < 0.0001$ (exact).